

The Cosmic Evolution of Binary Black Holes in Young, Globular and Nuclear Star Clusters: Rates, Masses, Spins and Mixing Fractions

Michela Mapelli^{1,2,3★}, Yann Bouffanais^{1,2}, Filippo Santoliquido^{1,2}, Manuel Arca Sedda⁴,
M. Celeste Artale⁵

¹*Physics and Astronomy Department Galileo Galilei, University of Padova, Vicolo dell'Osservatorio 3, I-35122, Padova, Italy*

²*INFN–Padova, Via Marzolo 8, I-35131 Padova, Italy*

³*INAF–Osservatorio Astronomico di Padova, Vicolo dell'Osservatorio 5, I-35122, Padova, Italy*

⁴*Astronomisches Rechen-Institut, Zentrum für Astronomie, Universität Heidelberg, Mönchhofstr. 12-14, Heidelberg, Germany*

⁵*Institut für Astro- und Teilchenphysik, Universität Innsbruck, Technikerstrasse 25/8, A-6020, Innsbruck, Österreich*

Accepted XXX. Received YYY; in original form ZZZ

ABSTRACT

The growing population of binary black holes (BBHs) observed by gravitational wave detectors is a potential Rosetta stone for understanding their formation channels. Here, we use an upgraded version of our semi-analytic codes `FASTCLUSTER` and `COSMORATE` to investigate the cosmic evolution of four different BBH populations: isolated BBHs and dynamically formed BBHs in nuclear star clusters (NSCs), globular clusters (GCs), and young star clusters (YSCs). We find that the merger rate density of BBHs in GCs and NSCs is barely affected by stellar metallicity (Z), while the rate of isolated BBHs changes wildly with Z . BBHs in YSCs behave in an intermediate way between isolated and GC/NSC BBHs. The local merger rate density of N th-generation black holes (BHs), obtained by summing up hierarchical mergers in GCs, NSCs and YSCs, ranges from ~ 1 to $\sim 4 \text{ Gpc}^{-3} \text{ yr}^{-1}$ and is mostly sensitive to the spin parameter. We find that the mass function of primary BHs evolves with redshift in GCs and NSCs, becoming more top-heavy at higher z . In contrast, the primary BH mass function almost does not change with redshift in YSCs and in the field. This signature of the BH mass function has relevant implications for Einstein Telescope and Cosmic Explorer. Finally, our analysis suggests that multiple channels contribute to the BBH population of the second gravitational-wave transient catalogue.

Key words: gravitational waves – black hole physics – stars: black holes – stars: kinematics and dynamics – galaxies: star clusters: general

1 INTRODUCTION

A variety of formation channels have been proposed for binary black holes (BBHs; see, e.g., Mapelli 2021 for a recent review): BBH mergers can be the outcome of isolated binary evolution via common envelope (Tutukov & Yungelson 1973; Bethe & Brown 1998; Portegies Zwart & Yungelson 1998; Belczynski et al. 2002, 2008, 2016a; Eldridge & Stanway 2016; Dvorkin et al. 2016, 2018; Stevenson et al. 2017; Mapelli et al. 2017, 2019; Kruckow et al. 2018; Spera et al. 2019; Tanikawa et al. 2021; Belczynski et al. 2020; Klencki et al. 2021; Olejak et al. 2021), stable mass transfer (Giacobbo et al. 2018; Neijssel et al. 2019; Bavera et al. 2020; Gallegos-Garcia et al. 2021) or chemically homogeneous evolution (Marchant et al. 2016; Mandel & de Mink 2016; de Mink & Mandel 2016; du Buisson et al. 2020; Riley et al. 2021). Alternatively, BBHs can form dynamically in triples (e.g., Antonini et al. 2017; Silsbee & Tremaine 2017; Arca Sedda et al. 2021b; Fragione & Silk 2020; Vigna-Gómez et al. 2021), young star clusters (YSCs, Banerjee et al. 2010; Mapelli 2016; Banerjee 2017, 2021; Di Carlo et al. 2019, 2020a; Kumamoto et al. 2019, 2020), globular clusters (GCs, Portegies Zwart & McMillan 2000;

Tanikawa 2013; Samsing et al. 2014; Rodriguez et al. 2016; Askar et al. 2017; Fragione & Kocsis 2018; Choksi et al. 2019; Hong et al. 2018; Kamlah et al. 2021), and nuclear star clusters (NSCs, Antonini & Rasio 2016; Petrovich & Antonini 2017; Antonini et al. 2019; Arca Sedda et al. 2020; Arca Sedda 2020; Fragione et al. 2020). Furthermore, gas torques in AGN discs trigger the formation of BBHs and speed up their mergers (e.g., Bartos et al. 2017; Stone et al. 2017; McKernan et al. 2018; Yang et al. 2019; Tagawa et al. 2020; Ishibashi & Gröbner 2020). Finally, primordial black holes (BHs), born from gravitational collapses in the early Universe, might also pair up and merge via gravitational wave (GW) emission (e.g., Carr & Hawking 1974; Carr et al. 2016; Sasaki et al. 2016; Ali-Haïmoud et al. 2017; Clesse & García-Bellido 2017; De Luca et al. 2021).

One of the key signatures of the dynamical scenario is the formation of massive BHs via hierarchical merger chains (Miller & Hamilton 2002; Giersz et al. 2015; Fishbach et al. 2017; Gerosa & Berti 2017; Rodriguez et al. 2019; Arca Sedda et al. 2021c; Mapelli et al. 2021; Gerosa & Fishbach 2021): the remnant of a BBH merger is a single object at birth, but, if it is inside a dense stellar environment, it may pair up dynamically with other BHs and merge again. The merger remnant has a distinctive feature, which is a large spin magnitude $\chi \sim 0.7$, mostly inherited from pre-merger orbital angular

★ E-mail: michela.mapelli@unipd.it

momentum (Jiménez-Forteza et al. 2017; Gerosa & Fishbach 2021). The efficiency of hierarchical mergers is hampered by relativistic kicks, that the merger remnant suffers at birth because of radiation of linear momentum through beamed GW emission (Fitchett 1983; Favata et al. 2004; Campanelli et al. 2007; Lousto & Zlochower 2011). The magnitude of the relativistic kick is generally comparable to (or higher than) the escape velocity of a massive star cluster, and can lead to the ejection of the merger remnant, interrupting the hierarchical chain (Holley-Bockelmann et al. 2008; Moody & Sigurdsson 2009).

Advanced LIGO (Aasi et al. 2015) and Virgo (Acernese et al. 2015) observed more than 50 BBH mergers to date (Abbott et al. 2021b,a). Population analyses on these BBHs moderately support the co-existence of multiple formation channels (Abbott et al. 2021c; Callister et al. 2020; Zevin et al. 2021; Wong et al. 2021; Bouffanais et al. 2021, but see Roulet et al. 2021 for a different result). Moreover, GW190521 (Abbott et al. 2020a,b), and possibly GW190403_051519 and GW190426_190642 (Abbott et al. 2021a) challenge current models of massive star evolution, hosting BHs in the pair-instability mass gap (Belczynski et al. 2016b; Woosley 2017; Spera & Mapelli 2017; Marchant et al. 2019; Stevenson et al. 2019; Farmer et al. 2019; Mapelli et al. 2020; Farrell et al. 2021; Vink et al. 2021; Costa et al. 2021; Tanikawa et al. 2021). The properties of these events are easier to explain with a dynamical scenario (Fragione & Silk 2020; Anagnostou et al. 2020; Kimball et al. 2020; Mapelli et al. 2021; Arca Sedda et al. 2021a; Liu & Lai 2021; Spera et al. 2019; Di Carlo et al. 2019, 2020a,b; Gerosa et al. 2021; Kremer et al. 2020b; Renzo et al. 2020; González et al. 2021) than with binary evolution (Belczynski 2020).

Several studies performed a multi-channel analysis, trying to constrain the relative contribution of each formation scenario to the observed BBH population (e.g., Zevin et al. 2017; Stevenson et al. 2017; Mandel et al. 2019; Bouffanais et al. 2019, 2021; Zevin et al. 2021; Wong et al. 2021). Models of different formation channels are generally produced with different numerical techniques: For example, BBHs in NSCs are generally studied with semi-analytical models (e.g., Antonini & Rasio 2016; Arca Sedda 2020), BBHs in GCs are often modelled with hybrid Monte Carlo simulations (e.g., Rodríguez et al. 2016; Askar et al. 2017), BBHs in YSCs with direct N-body simulations (e.g., Banerjee et al. 2010; Ziosi et al. 2014; Fujii & Portegies Zwart 2014) and isolated BBHs with population-synthesis simulations (e.g., Belczynski et al. 2016a; Mapelli et al. 2017; Eldridge & Stanway 2016), run with different codes and assumptions. Comparing catalogs of BBHs simulated with different codes might lead to biased results: the differences among the considered BBH catalogs might be due to the adopted numerical approach rather than to the intrinsic physical differences among channels (e.g., Belczynski et al. 2021). For example, if the assumed initial BH mass function is different for different models, the results of the multi-channel comparison will be conditioned by this discrepancy in the initial conditions. The only way to avoid such bias is to simulate different dynamical channels with the same numerical code, starting from the same underlying initial conditions (e.g., the same BH mass function). At present, this cannot be done with direct N-body simulations, because of their high computational cost, especially for the most massive and long-lived star clusters (Wang 2020).

The purpose of this work is to compare the merger rate and other BBH properties (mass and spin distribution) we obtain for different channels, by adopting the same numerical code for all the considered scenarios. We use the semi-analytic dynamical code `FASTCLUSTER` (Mapelli et al. 2021), which can handle isolated BBHs and dynamical BBHs in YSCs, GCs and NSCs within the same numerical framework. `FASTCLUSTER` overcomes the numerical challenge of simulating

BBHs in massive and long-lived star clusters by integrating the effect of dynamical hardening and GW emission with a fast semi-analytic approach, calibrated on direct N-body models. Finally, we derive the mixing fraction of each channel, by running Bayesian hierarchical inference on the public data of the second GW transient catalog (GWTC-2, Abbott et al. 2021b).

2 METHODS

2.1 Isolated BBHs

Isolated BBHs form and evolve in the field; they are not perturbed by dynamical interactions. To generate masses, delay times¹ and spin orientations of isolated BBHs, we use the population-synthesis code `MOBSE` (Giacobbo et al. 2018; Giacobbo & Mapelli 2018). Dimensionless spin magnitudes χ are randomly drawn from a Maxwellian distribution truncated to $\chi = 1$, with root mean square $\sigma_\chi = 0.1$ (fiducial case) or $\sigma_\chi = 0.01$ (low-spin case).

`MOBSE` is an upgraded and custom version of `BSE` (Hurley et al. 2002). It implements up-to-date models for stellar winds (Vink et al. 2001; Gräfener & Hamann 2008; Chen et al. 2015), core-collapse supernovae (SNe, Fryer et al. 2012), pair-instability SNe (Mapelli et al. 2020) and SN kicks (Giacobbo & Mapelli 2020). For more details, we refer to Giacobbo et al. (2018) and Giacobbo & Mapelli (2018). BHs with mass up to $\approx 65 M_\odot$ can form from metal-poor stars in `MOBSE`, but only BHs with mass up to $\approx 45 M_\odot$ merge within a Hubble time in isolated binary systems (see, e.g., Figure 11 of Giacobbo & Mapelli 2018). The main reason of this difference is that tight isolated binary stars, which are the progenitors of isolated BBH mergers, evolve via mass transfer or common envelope. These are dissipative processes and lead to the complete removal of stellar envelopes, leaving behind naked He cores. The maximum mass of a BH that forms from a naked He core is $\approx 45 M_\odot$ in `MOBSE` models.

2.2 First generation (1g) BBHs in star clusters

To generate catalogs of BBH mergers in dynamical environments (YSCs, GCs and NSCs), we use the semi-analytic code `FASTCLUSTER` (Mapelli et al. 2021). Here below, we summarize the main features of this code and refer to Mapelli et al. (2021) for more details. `FASTCLUSTER` takes into account two classes of BBHs: original and dynamical BBHs. The former originate from binary stars that are already present in the initial conditions (hereafter, original binaries), while the latter are dynamically assembled. Both original and dynamical BBHs evolve inside their parent star cluster and are affected by dynamical encounters.

A dynamical BBH forms in a timescale

$$t_{\text{dyn}} = \max [t_{\text{SN}}, t_{\text{DF}} + \min (t_{3\text{bb}}, t_{12})], \quad (1)$$

where t_{SN} is the time of the core-collapse SN explosion or direct collapse, t_{DF} is the dynamical friction timescale (Chandrasekhar 1943), $t_{3\text{bb}}$ is the timescale for dynamical formation of a BBH via three-body encounters (Goodman & Hut 1993; Lee 1995) and t_{12} is the timescale for dynamical formation of a BBH via exchange into an existing binary star (Miller & Lauburg 2009). For the aforementioned

¹ The delay time is the time between the formation of a binary star and the merger of the final BBH.

timescales, we use the following approximations:

$$t_{\text{DF}} = \frac{3}{4(2\pi)^{1/2}} \frac{\sigma^3}{G^2 \ln \Lambda m_{\text{BH}} \rho},$$

$$t_{3\text{bb}} = 125 \text{ Myr} \left(\frac{10^6 M_{\odot} \text{ pc}^{-3}}{\rho_c} \right)^2 \left(\zeta^{-1} \frac{\sigma_{1\text{D}}}{30 \text{ km s}^{-1}} \right)^9 \left(\frac{20 M_{\odot}}{m_{\text{BH}}} \right)^5,$$

$$t_{12} = 3 \text{ Gyr} \left(\frac{0.01}{f_{\text{bin}}} \right) \left(\frac{10^6 M_{\odot} \text{ pc}^{-3}}{\rho_c} \right) \left(\frac{\sigma}{50 \text{ km s}^{-1}} \right) \left(\frac{12 M_{\odot}}{m_{\text{BH}} + 2 m_*} \right) \left(\frac{1 \text{ AU}}{a_{\text{hard}}} \right), \quad (2)$$

where G is the gravity constant, m_{BH} is the mass of the BH, σ is the 3D velocity dispersion, ρ is the mass density at the half-mass radius, $\ln \Lambda \sim 10$ is the Coulomb logarithm, ρ_c is the central density of the star cluster, $\sigma_{1\text{D}} = \sigma/\sqrt{3}$ is the one-dimensional velocity dispersion at the half-mass radius (assuming an isotropic distribution of stellar velocities) and $\zeta \leq 1$ accounts for deviations from equipartition of a BH subsystem (here we assume that there is equipartition, Spitzer 1969). Furthermore, f_{bin} is the binary fraction, m_* is the average mass of a star in the cluster and $a_{\text{hard}} = G m_*/\sigma^2$ is the minimum semi-major axis of a hard binary system. Equation 1 indicates that a dynamical BBH forms only after the primary BH had enough time to sink to the cluster core by dynamical friction and acquire a companion via either three-body or exchange interactions.

The masses of both original and dynamical BBHs are generated from the population-synthesis code MOBSE (Giacobbo et al. 2018; Giacobbo & Mapelli 2018). FASTCLUSTER can take any other possible initial conditions for BH masses. However, this choice ensures that the underlying BH mass spectrum is the same for isolated, original and dynamical BBHs. The main difference between original and dynamical BBHs is that the masses of original BBHs are taken from isolated BBH simulations (they are the same as isolated BBHs), while the masses of dynamical BBHs are extracted from the distribution of single BHs. The secondary component mass of a dynamical BBH is extracted from a distribution $p(m_2) \propto (m_1 + m_2)^4$, where m_1 and m_2 are the primary and secondary component, respectively (O’Leary et al. 2016).

Consistently with isolated BBHs, BH spin magnitudes are randomly sampled from a Maxwellian distribution with root mean square $\sigma_{\chi} = 0.1$ (fiducial case) or $\sigma_{\chi} = 0.01$ (low-spin case). We randomly draw spin directions isotropic over the sphere, because dynamics resets any spin alignments.

The semi-major axis a and the eccentricity e at the time of BBH formation are calculated with MOBSE in the case of original BBHs and are drawn from the following probability distributions in the case of dynamical BBHs (Heggie 1975):

$$p(a) \propto a^{-1} \quad a \in [1, 10^3] R_{\odot}$$

$$p(e) = 2e \quad e \in [0, 1). \quad (3)$$

At the beginning of the integration, we check if a (dynamical or original) BBH is hard, i.e. if its binding energy E_b satisfies the following relationship (Heggie 1975)

$$E_b = \frac{G m_1 m_2}{2a} \geq \frac{1}{2} m_* \sigma^2. \quad (4)$$

If the binary is hard, we integrate its orbital evolution. Otherwise, we assume it breaks via dynamical encounters.

2.3 Orbital evolution

When a BBH is hard and is inside its parent star cluster, the evolution of its semi-major axis a and eccentricity e can be described as

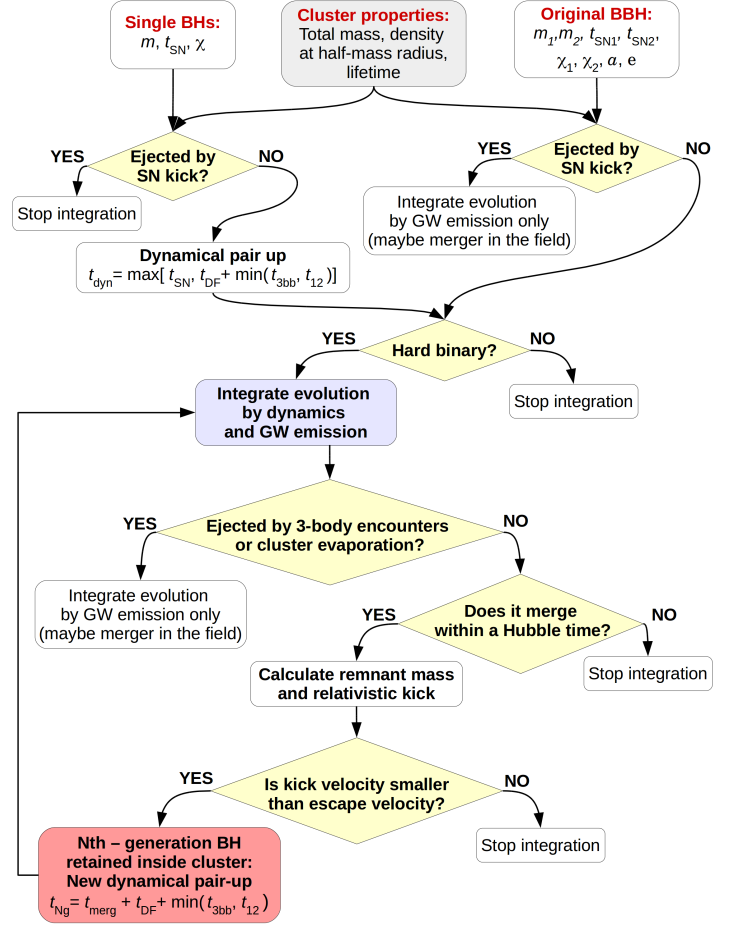


Figure 1. Flow chart of FASTCLUSTER.

(Mapelli 2021):

$$\frac{da}{dt} = -2\pi \xi \frac{G \rho_c}{\sigma} a^2 - \frac{64}{5} \frac{G^3 m_1 m_2 (m_1 + m_2)}{c^5 a^3 (1 - e^2)^{7/2}} f_1(e)$$

$$\frac{de}{dt} = 2\pi \xi \kappa \frac{G \rho_c}{\sigma} a - \frac{304}{15} e \frac{G^3 m_1 m_2 (m_1 + m_2)}{c^5 a^4 (1 - e^2)^{5/2}} f_2(e), \quad (5)$$

where c is the speed of light and (Peters 1964)

$$f_1(e) = \left(1 + \frac{73}{24} e^2 + \frac{37}{96} e^4 \right)$$

$$f_2(e) = \left(1 + \frac{121}{304} e^2 \right). \quad (6)$$

In eqs. 5, ξ and κ are two dimensionless parameters, calibrated with direct N-body simulations (Hills 1983; Quinlan 1996; Miller & Hamilton 2002; Sesana et al. 2006). Here, we assume $\xi = 3$ (Quinlan 1996) and $\kappa = 0.1$ (Sesana et al. 2006). Equations 5 are composed of two terms. The first ones ($\frac{da}{dt} \propto -a^2$ and $\frac{de}{dt} \propto a$) describe the dynamical hardening and the evolution of eccentricity via Newtonian dynamical scatterings; the second ones ($\frac{da}{dt} \propto -a^{-3}$ and $\frac{de}{dt} \propto -a^{-4}$) describe hardening and circularization via GW emission (Peters 1964).

FASTCLUSTER integrates eqs. 5 until the BBH is ejected from the cluster, or it merges, or the star cluster dies by evaporation, or we reach the Hubble time (which one of these cases happens first). If

the BBH is ejected from the cluster, `FASTCLUSTER` integrates only the second terms of eqs. 5 (hardening and circularization by GW emission) until either the BBH merges in the field or a Hubble time has elapsed.

A binary is assumed to be ejected from the cluster when $a_{\text{ej}} > a_{\text{GW}}$ (Baibhav et al. 2020) with

$$a_{\text{ej}} = \frac{2 \xi m_*^2}{(m_1 + m_2)^3} \frac{G m_1 m_2}{v_{\text{esc}}^2} \quad (7)$$

$$a_{\text{GW}} = \left[\frac{32 G^2}{5 \pi \xi c^5} \frac{\sigma m_1 m_2 (m_1 + m_2)}{\rho_c (1 - e^2)^{7/2}} f_1(e) \right]^{1/5}.$$

The former of the two eqs. 7 describes the semi-major axis below which the BBH is ejected by dynamical recoil, while the latter describes the maximum semi-major axis for the regime of efficient orbital decay via GW emission.

2.4 Nth generation (Ng) dynamical BBHs

If the BBH merges in less than a Hubble time, we estimate the mass and spin of the merger remnant using the fitting formulas by Jiménez-Forsteza et al. (2017). If the BBH merges inside its parent star cluster, we also calculate the relativistic kick magnitude v_{K} using the fit by Lousto et al. (2012). We assume that the merger remnant remains inside its parent cluster if the relativistic kick magnitude $v_{\text{K}} < v_{\text{esc}}$, where v_{esc} is the escape velocity from the star cluster. Otherwise, the merger remnant is ejected from the parent cluster and cannot participate in any further hierarchical mergers.

Even when the merger remnant remains inside its parent cluster, the kick sends it far away from the cluster core. The BH must sink back to the core via dynamical friction before it can acquire new companions via three-body encounters or exchanges. We then calculate the timescale t_{Ng} for the merger remnant to pair up dynamically with a new companion BH as

$$t_{\text{Ng}} = t_{\text{merg}} + t_{\text{DF}} + \min(t_{3\text{bb}}, t_{12}). \quad (8)$$

In the above equation, $t_{\text{merg}} = t_{\text{dyn}} + t_{\text{GW}}$ is the delay time of the first generation (1g) BBH (where t_{dyn} is defined in eq. 1, while t_{GW} is the time elapsed from the formation of the BBH to its merger, according to eqs. 5). If t_{Ng} is shorter than the Hubble time, we start the loop again by integrating the second generation (2g) BBH with Eqs 5. We iterate the hierarchical merger chain until the merger remnant is ejected from the cluster, or the cluster evaporates, or we reach the Hubble time. Figure 1 is a flow chart of `FASTCLUSTER`.

2.5 Properties of star clusters

We consider three different flavours of star clusters: NSCs, GCs and YSCs. Each star cluster is uniquely defined by its lifetime t_{SC} , total mass M_{tot} , binary fraction f_{bin} and half-mass density ρ . We assume $t_{\text{SC}} = 13.6, 13.6$ and 1 Gyr for NSCs, GCs (Gratton et al. 1997, 2003; VandenBerg et al. 2013) and YSCs (Portegies Zwart et al. 2010), respectively. Furthermore, we assume $f_{\text{bin}} = 0.01, 0.1$ and 1 in NSCs (Antonini & Rasio 2016), GCs (Ji & Bregman 2015) and YSCs (Sana et al. 2012), respectively. We draw the total masses from a log-normal distribution with mean $\langle \log_{10} M_{\text{tot}}/M_{\odot} \rangle = 6.18, 5.6$ and 4.3 for NSCs, GCs and YSCs, respectively. We assume a fiducial standard deviation $\sigma_{\text{M}} = 0.4$ for all star cluster flavours. We draw the density at the half-mass radius from a log-normal distribution with mean $\langle \log_{10} \rho/(M_{\odot} \text{pc}^{-3}) \rangle = 5, 3.7$ and 3.3 for NSCs, GCs and YSCs, respectively. We assume a fiducial standard deviation $\sigma_{\rho} = 0.4$ for all star cluster flavours. The values of M_{tot} and ρ are

inferred from the observations reported in Neumayer et al. (2020) for NSCs and GCs (see also Harris 1996; Georgiev et al. 2016) and from Portegies Zwart et al. (2010) for YSCs. For each star cluster, we assume a core density $\rho_c = 20 \rho$. We derive the escape velocity from M_{tot} and ρ (Georgiev et al. 2009a,b; Fragione & Silk 2020) using the following relationship

$$v_{\text{esc}} = 40 \text{ km s}^{-1} \left(\frac{M_{\text{tot}}}{10^5 M_{\odot}} \right)^{1/3} \left(\frac{\rho}{10^5 M_{\odot} \text{pc}^{-3}} \right)^{1/6}. \quad (9)$$

Equation 9 results in a distribution of escape velocities fairly consistent with the observational sample reported in Figure 1 of Antonini & Rasio (2016) for GCs and NSCs. In the initial conditions, we generate each star cluster by randomly drawing a value of M_{TOT} and ρ from the aforementioned distributions. We simulate only one BBH per each randomly drawn star cluster, in order to better sample the parameter space of BBHs and possible host clusters. Here, we do not consider NSCs that host a supermassive BH. In such clusters, most of the binaries inside the influence radius of the supermassive BH are soft. We refer to Arca Sedda (2020) for a detailed treatment of this case. We assume, for the sake of simplicity, that the star cluster properties do not evolve in time. We will add the evolution of the star cluster in a follow-up study.

2.6 BBH merger rate

The BBH merger rate per each channel i can be estimated as

$$\mathcal{R}_i(z) = \frac{d}{dt(z)} \int_{z_{\text{max}}}^z \psi_i(z') \frac{dt(z')}{dz'} dz' \int_{Z_{\text{min}}(z')}^{Z_{\text{max}}(z')} \eta_i(Z) \mathcal{F}_i(z', z, Z) dZ, \quad (10)$$

where $t(z)$ is the look-back time at redshift z , $\psi_i(z')$ is the formation rate density at redshift z' for the i -th channel, where $i = \text{NSCs, GCs, YSCs or field}$, $Z_{\text{min}}(z')$ and $Z_{\text{max}}(z')$ are the minimum and maximum metallicity of stars formed at redshift z' , $\eta_i(Z)$ is the merger efficiency at metallicity Z , and $\mathcal{F}_i(z', z, Z)$ is the fraction of BBHs belonging to a given channel i that form at redshift z' from stars with metallicity Z and merge at redshift z , normalized to all BBHs belonging to the same channel i that form from stars with metallicity Z . To calculate the look-back time we take the cosmological parameters (H_0, Ω_{M} and Ω_{Λ}) from Ade et al. (2016).

2.6.1 Formation rate density

In our fiducial model, we define $\psi_i(z)$ as follows. For the formation rate of GCs as a function of redshift we assume a Gaussian distribution

$$\psi_{\text{GC}}(z) = \mathcal{B}_{\text{GC}} \exp \left[-(z - z_{\text{GC}})^2 / (2 \sigma_{\text{GC}}^2) \right], \quad (11)$$

where, in the fiducial model, $z_{\text{GC}} = 3.2$ is the redshift where the formation rate of GCs is maximum, $\sigma_{\text{GC}} = 1.5$ is the standard deviation of the distribution and \mathcal{B}_{GC} is the normalization factor. This distribution is reminiscent of the one estimated by El-Badry et al. (2019) (see also Rodríguez & Loeb 2018). In particular, the fiducial normalization we adopt, $\mathcal{B}_{\text{GC}} = 2 \times 10^{-4} M_{\odot} \text{Mpc}^{-3} \text{yr}^{-1}$, is consistent with both El-Badry et al. (2019) and Reina-Campos et al. (2019). The peak redshift $z_{\text{GC}} = 3.2$ is not taken from El-Badry et al. (2019), who report $z_{\text{GC}} = 4$, but rather is calibrated on the distribution of the ages of Galactic GCs, which peaks at $z = 3.2$ (Gratton et al. 1997, 2003; VandenBerg et al. 2013). In Section 4, we will discuss the impact of these parameters on the merger rate. If

we assume that none of our GCs dies by evaporation, eq. 11 yields a density of GCs in the local Universe $n_{\text{GC}} \approx 4 \text{ Mpc}^{-3}$. This is higher than the observed value ($n_{\text{GC}} \approx 2.5 \text{ Mpc}^{-3}$, Portegies Zwart & McMillan 2000), but our estimate of n_{GC} must be regarded as an upper limit because we assume that all GCs, even the least massive, survive to redshift zero. Fig. 2 shows the formation rate density as a function of redshift for the four channels considered here.

The uncertainty on the formation rate of NSCs is even higher. According to several models (Tremaine et al. 1975; Capuzzo-Dolcetta 1993; Capuzzo-Dolcetta & Miocchi 2008; Antonini et al. 2012), NSCs form from the merger of GCs sinking to the centre of their host galaxies by dynamical friction. Thus, for NSCs we adopt the same functional form as for GC formation history, but we reduce the normalization:

$$\psi_{\text{NSC}}(z) = \mathcal{B}_{\text{NSC}} \exp \left[-(z - z_{\text{NSC}})^2 / (2\sigma_{\text{NSC}}^2) \right], \quad (12)$$

where, in the fiducial model, $z_{\text{NSC}} = 3.2$ and $\sigma_{\text{NSC}} = 1.5$ for analogy with GCs. This formalism is subject to large uncertainties, because of the scarce observational constraints. In Section 4, we will comment on these uncertainties. In our fiducial model, the normalization of eq. 12 is $\mathcal{B}_{\text{NSC}} = 10^{-5} \text{ M}_{\odot} \text{ Mpc}^{-3} \text{ yr}^{-1}$, and was chosen so that we obtain a NSC density in the local Universe comparable with the observed one. If we assume that all NSCs survive to redshift zero (which is reasonable for NSCs) and integrate eq. 12 over cosmic time, we find a current density of NSCs $n_{\text{NSC}} \approx 0.06 \text{ Mpc}^{-3}$. For comparison, if we take the density of galaxies with stellar mass $> 10^7 \text{ M}_{\odot}$ from observations (Conselice et al. 2016) and assume that all such galaxies have a NSC, we expect a current NSC density $n_{\text{NSC}} \approx 0.05 - 0.1 \text{ Mpc}^{-3}$, which compares nicely with our estimate.

Modelling the redshift evolution of YSCs is a somewhat easier task, because YSCs are expected to trace the total cosmic star formation rate density (Lada & Lada 2003; Portegies Zwart et al. 2010). Hence, we assume

$$\psi_{\text{YSC}}(z) = \mathcal{B}_{\text{YSC}}(z) \psi(z), \quad (13)$$

where

$$\psi(z) = 0.01 \frac{(1+z)^{2.6}}{1 + [(1+z)/3.2]^{6.2}} \text{ M}_{\odot} \text{ Mpc}^{-3} \text{ yr}^{-1} \quad (14)$$

is the fit to the total cosmic star formation rate density by Madau & Fragos (2017) and $\mathcal{B}_{\text{YSC}}(z)$ is the fraction of the cosmic star formation rate density that happens in YSCs. In our fiducial model, we adopt

$$\mathcal{B}_{\text{YSC}}(z) = \min \left(0.1, 1 - \frac{\psi_{\text{NSC}}(z)}{\psi(z)} - \frac{\psi_{\text{GC}}(z)}{\psi(z)} \right). \quad (15)$$

In the above equation, we assume that YSCs represent $\sim 10\%$ of the total cosmic star formation rate, as a reasonable guess from Kruijssen (2014) and impose that the total star formation rate density in our model at a given redshift cannot be higher than $\psi(z)$.

Finally, the star formation rate in the field will be equal to the remaining portion of the total cosmic star formation rate density:

$$\psi_{\text{iso}}(z) = \mathcal{B}_{\text{iso}}(z) \psi(z), \quad (16)$$

where

$$\mathcal{B}_{\text{iso}}(z) = 1 - \frac{\psi_{\text{NSC}}(z)}{\psi(z)} - \frac{\psi_{\text{GC}}(z)}{\psi(z)} - \frac{\psi_{\text{YSC}}(z)}{\psi(z)}. \quad (17)$$

The star formation rate in the field is dominant over the other channels in our fiducial model, as shown in Fig. 2.

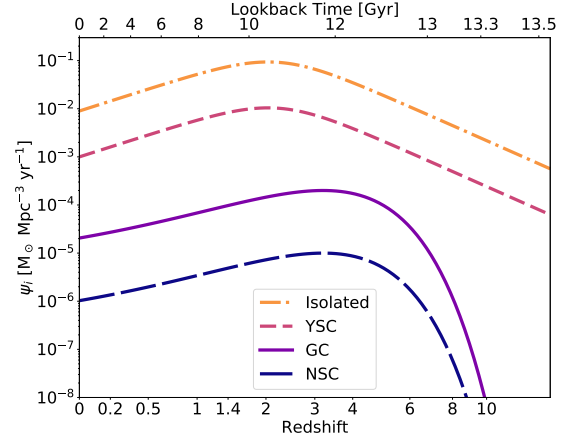


Figure 2. Star formation rate density as a function of redshift for isolated stars (orange dot-dashed line), YSCs (magenta short-dashed line), GCs (violet solid line) and NSCs (blue long-dashed line).

2.6.2 Merger efficiency

The merger efficiency is the total number of BBHs of a given population that merge within a Hubble time divided by the total initial stellar mass of that population (Giacobbo et al. 2018; Klencik et al. 2018). For isolated BBHs, this is simply

$$\eta_{\text{field}}(Z) = \frac{N_{\text{TOT}}(Z)}{M_*(Z)}, \quad (18)$$

where $N_{\text{TOT}}(Z)$ is the number of BBH mergers for a given metallicity Z and $M_*(Z)$ is the total initial stellar mass of the population, assuming a Kroupa mass function between 0.1 and 150 M_{\odot} (Kroupa 2001).

For dynamical and original BBHs, the calculation of $\eta(Z)$ is less straightforward, because FASTCLUSTER does not integrate the entire BH population of a star cluster, but only a sub-set, in order to sample the parameter space more efficiently (see Section 2.5). We thus estimate the merger efficiency in star clusters as

$$\eta_{\text{SC}}(Z) = \frac{N_{\text{merg, sim}}(Z)}{N_{\text{sim}}(Z)} \frac{N_{\text{BH}}(Z)}{M_*(Z)}, \quad (19)$$

where $N_{\text{merg, sim}}(Z)$ is the number of BHs simulated with FASTCLUSTER that merge within a Hubble time for a given metallicity Z , $N_{\text{sim}}(Z)$ is the number of BHs simulated with FASTCLUSTER for a given metallicity Z , N_{BH} is the total number of BHs associated with a given metallicity (including the BHs we did not simulate with FASTCLUSTER) and $M_*(Z)$ is the total initial stellar mass for a given metallicity Z . $N_{\text{merg, sim}}(Z)$ and $N_{\text{sim}}(Z)$ are directly extracted from the simulations. We calculate $M_*(Z) = \sum M_{\text{TOT}}(Z)$, i.e. the sum of the initial total mass of all simulated star clusters with a given Z . We derive $N_{\text{BH}}(Z)$ as the number of BHs we expect from a stellar population following a Kroupa mass function between 0.1 and 150 M_{\odot} , assuming that all stars with zero-age main sequence mass $\geq 20 \text{ M}_{\odot}$ are BH progenitors (Heger et al. 2003). In our definition, $N_{\text{merg, sim}}(Z)$ includes even N th generation (N_g) mergers, while $N_{\text{sim}}(Z)$ counts only 1g BHs. Hence, the ratio $N_{\text{merg, sim}}(Z)/N_{\text{sim}}(Z)$ can be > 1 if hierarchical mergers are extremely efficient.

[h]

Table 1. Model properties.

Model	Channel	SN model	α	σ_χ	σ_Z	f_{orig}
A02	Isolated	delayed	1	0.1	0.2	1
A02	YSC	delayed	1	0.1	0.2	0.6
A02	GC	delayed	1	0.1	0.2	0.1
A02	NSC	delayed	1	0.1	0.2	0.01
A03	Isolated	delayed	1	0.1	0.3	1
A03	YSC	delayed	1	0.1	0.3	0.6
A03	GC	delayed	1	0.1	0.3	0.1
A03	NSC	delayed	1	0.1	0.3	0.01
A04	Isolated	delayed	1	0.1	0.4	1
A04	YSC	delayed	1	0.1	0.4	0.6
A04	GC	delayed	1	0.1	0.4	0.1
A04	NSC	delayed	1	0.1	0.4	0.01
B02	Isolated	rapid	1	0.1	0.2	1
B02	YSC	rapid	1	0.1	0.2	0.6
B02	GC	rapid	1	0.1	0.2	0.1
B02	NSC	rapid	1	0.1	0.2	0.01
B03	Isolated	rapid	1	0.1	0.3	1
B03	YSC	rapid	1	0.1	0.3	0.6
B03	GC	rapid	1	0.1	0.3	0.1
B03	NSC	rapid	1	0.1	0.3	0.01
B04	Isolated	rapid	1	0.1	0.4	1
B04	YSC	rapid	1	0.1	0.4	0.6
B04	GC	rapid	1	0.1	0.4	0.1
B04	NSC	rapid	1	0.1	0.4	0.01
C02	Isolated	delayed	1	0.01	0.2	1
C02	YSC	delayed	1	0.01	0.2	0.6
C02	GC	delayed	1	0.01	0.2	0.1
C02	NSC	delayed	1	0.01	0.2	0.01
C03	Isolated	delayed	1	0.01	0.3	1
C03	YSC	delayed	1	0.01	0.3	0.6
C03	GC	delayed	1	0.01	0.3	0.1
C03	NSC	delayed	1	0.01	0.3	0.01
C04	Isolated	delayed	1	0.01	0.4	1
C04	YSC	delayed	1	0.01	0.4	0.6
C04	GC	delayed	1	0.01	0.4	0.1
C04	NSC	delayed	1	0.01	0.4	0.01
D02	Isolated	delayed	5	0.1	0.2	1
D02	YSC	delayed	5	0.1	0.2	0.6
D02	GC	delayed	5	0.1	0.2	0.1
D02	NSC	delayed	5	0.1	0.2	0.01
D03	Isolated	delayed	5	0.1	0.3	1
D03	YSC	delayed	5	0.1	0.3	0.6
D03	GC	delayed	5	0.1	0.3	0.1
D03	NSC	delayed	5	0.1	0.3	0.01
D04	Isolated	delayed	5	0.1	0.4	1
D04	YSC	delayed	5	0.1	0.4	0.6
D04	GC	delayed	5	0.1	0.4	0.1
D04	NSC	delayed	5	0.1	0.4	0.01

Column 1: Name of the model, composed of a letter (A, B, C and D) followed by a number indicating the metallicity spread (02, 03 and 04 indicate $\sigma_Z = 0.2, 0.3$ and 0.4 , respectively); Column 2: formation channel (isolated, YSC, GC or NSC); Column 3: core-collapse SN model (delayed or rapid); Column 4: parameter α of common envelope for isolated binaries and original binaries; Column 5: spin parameter $\sigma_\chi = 0.1$ or 0.01 ; Column 6: metallicity spread $\sigma_Z = 0.2, 0.3, 0.4$; Column 7 (f_{orig}): original BBH fraction (in the isolated channel every binary is original).

2.6.3 Metallicity evolution

For the metallicity evolution, we adopt a formalism similar to the one described by [Bouffanais et al. \(2021\)](#), namely we use the fit to the mass-weighted metallicity evolution given by [Madau & Fragos \(2017\)](#):

$$\log \langle Z/Z_\odot \rangle = 0.153 - 0.074 z^{1.34} \quad (20)$$

To describe the spread around the mass-weighted metallicity, we assume that metallicities are distributed according to a log-normal distribution:

$$p(z', Z) = \frac{1}{\sqrt{2\pi\sigma_Z^2}} \exp \left\{ -\frac{[\log(Z(z')/Z_\odot) - \langle \log Z(z')/Z_\odot \rangle]^2}{2\sigma_Z^2} \right\}, \quad (21)$$

where

$$\langle \log Z(z')/Z_\odot \rangle = \log \langle Z(z')/Z_\odot \rangle - \frac{\ln(10)\sigma_Z^2}{2}. \quad (22)$$

The standard deviation σ_Z is highly uncertain. Here, we probe different values of $\sigma_Z = 0.2, 0.3$ and 0.4 . Equation 21 allows us to estimate the term $\mathcal{F}_i(z', z, Z)$ of eq. 10:

$$\mathcal{F}_i(z', z, Z) = \frac{\mathcal{N}_i(z', z, Z)}{\mathcal{N}_{\text{TOT},i}(Z)} p(z', Z), \quad (23)$$

where $\mathcal{N}_i(z', z, Z)$ is the total number of BBHs of channel i that form at redshift z' with metallicity Z and merge at redshift z , while $\mathcal{N}_{\text{TOT},i}(Z)$ is the total number of BBH mergers of channel i with progenitor's metallicity Z . We use the same metallicity formalism for all the considered channels.

2.6.4 Fraction of original and dynamical BBHs

With `FASTCLUSTER`, we evaluate original BBHs (i.e., BBHs that form from a binary star but then evolve dynamically in a star cluster) and dynamical BBHs (i.e., BBHs that form via three-body encounters or exchanges), separately. In order to estimate the total BBH merger rate, we need to know the percentage of original and dynamical BBHs. Ideally, the mixing fraction between original and dynamical BBHs can be obtained by running Bayesian inference on GWTC-2. However, this would significantly increase the number of dimensions of our multi-channel analysis (see the next section); hence, we prefer to assume some physically motivated guess for the fraction of original BBHs.

In NSCs, the fraction of original binaries surviving dynamical interactions is expected to be of the order of ~ 0.01 , because most binary systems are soft in such extreme environment ([Antonini & Rasio 2016](#)). Hence, we assume that the fraction of original BBHs in NSCs is ~ 0.01 , analogous to the total surviving binary fraction. We also assume that the fraction of original BBHs in GCs is ~ 0.1 , corresponding to the typical binary fraction measured in the core of GCs, with large fluctuations from cluster to cluster ([Sollima et al. 2007](#); [Milone et al. 2012](#)). For YSCs we use the recent results by [Di Carlo et al. \(2020b\)](#) and [Rastello et al. \(2021\)](#). Based on direct N-body simulations of YSCs, they find that the percentage of original BBH mergers is $\approx 60\%$, with large fluctuations depending on metallicity. In Section 4, we will comment on the impact of these assumptions about the original BBH merger fraction. Finally, in the isolated BBH channel, each BBH is original by definition. The only difference between isolated BBHs and original binaries in YSCs/GCs/NSCs is that the latter are perturbed by dynamical encounters, while the former are unperturbed.

2.7 Description of runs

For the isolated BBH channel, we ran 1.44×10^8 massive isolated binary systems with MOBSE, considering twelve different metallicities ($Z = [0.0002, 0.0004, 0.0008, 0.0012, 0.0016, 0.002, 0.004, 0.006, 0.008, 0.012, 0.016, 0.02]$), two different SN models (rapid and delayed model, from Fryer et al. 2012) and two values for the parameter α of common envelope ($\alpha = 1, 5$). The zero-age main-sequence masses of the primary component of each binary star are distributed according to a Kroupa (Kroupa 2001) initial mass function in the range $[5, 150] M_\odot$. The orbital periods, eccentricities and mass ratios of binaries are drawn from Sana et al. (2012). In particular, we derive the mass ratio q as $\mathcal{F}(q) \propto q^{-0.1}$ with $q \in [0.1, 1]$, the orbital period P from $\mathcal{F}(\Pi) \propto \Pi^{-0.55}$ with $\Pi = \log(P/\text{day}) \in [0.15, 5.5]$ and the eccentricity e from $\mathcal{F}(e) \propto e^{-0.42}$ with $0 \leq e \leq 0.9$.

For the dynamical channels, we ran 288 different realizations of our models with FASTCLUSTER, half of them for original binaries and the other half for dynamical binaries. Each of these 288 realizations consists of 10^6 BBH systems. We consider three families of star clusters (NSCs, GCs and YSCs), twelve metallicities (the same as for the isolated BBHs), two values of the spin magnitude parameter ($\sigma_\chi = 0.01$ and 0.1), two core-collapse SN models (rapid and delayed model, from Fryer et al. 2012) and two values for the parameter α of common envelope ($\alpha = 1, 5$). The properties of the star clusters are the same as described in Section 2.5.

For each of the isolated and dynamical models, we ran the COSMORATE code, in order to derive the merger rate of each specific channel. We considered three values of the metallicity spread $\sigma_Z = 0.2, 0.3$ and 0.4 . Table 1 summarizes the details of each resulting model. Each model presented in Table 1 includes the 12 simulated progenitor metallicities, mixed according to the formalism of COSMORATE (Section 2.6). Furthermore, each star cluster model in Table 1 includes both dynamical and original BBHs, mixed according to the fractions described in Section 2.6.4. In Section 4, we will consider additional models with respect to the ones summarized in Table 1, to discuss the main uncertainties related to the formation rate of each channel, to the proportion between original and dynamical BBHs and to the properties of the considered star clusters.

2.8 Bayesian inference and mixing fractions

To compare our models against GW events in the first (O1), second (O2) and in the first part of the third observing run (O3a) of the LIGO–Virgo collaboration (LVC), we use a hierarchical Bayesian approach. Given a number N_{obs} of GW observations, $\mathcal{H} = \{h^k\}_{k=1}^{N_{\text{obs}}}$, described by an ensemble of parameters θ , the posterior distribution of the hyper-parameters λ associated with the models is described as an in-homogeneous Poisson distribution (Loredo 2004; Mandel et al. 2019)

$$p(\lambda, N_\lambda | \mathcal{H}) = e^{-\mu_\lambda} \pi(\lambda, N_\lambda) \prod_{k=1}^{N_{\text{obs}}} N_\lambda \int_{\theta} \mathcal{L}^k(h^k | \theta) p(\theta | \lambda) d\theta, \quad (24)$$

where θ are the GW parameters, N_λ is the number of events predicted by the astrophysical model, μ_λ is the predicted number of detections associated with the model and the GW detector, $\pi(\lambda, N_\lambda)$ is the prior distribution on λ and N_λ , and $\mathcal{L}^k(\{h\}^k | \theta)$ is the likelihood of the k -th detection. The predicted number of detections is given by $\mu(\lambda) = N_\lambda \beta(\lambda)$, where

$$\beta(\lambda) = \int_{\theta} p(\theta | \lambda) p_{\text{det}}(\theta) d\theta \quad (25)$$

Table 2. BBH merger rate density at redshift $z = 0$.

Model	Channel	$\mathcal{R}(0)$	$\mathcal{R}_{\text{Ng}}(0)$
A02	Isolated	5.14	–
A02	YSC	2.35	0.07
A02	GC	3.64	0.82
A02	NSC	1.31	0.47
A03	Isolated	17.53	–
A03	YSC	4.40	0.11
A03	GC	4.58	0.98
A03	NSC	1.41	0.51
A04	Isolated	60.67	–
A04	YSC	8.72	0.16
A04	GC	5.59	1.14
A04	NSC	1.50	0.54
B02	Isolated	7.41	–
B02	YSC	3.10	0.08
B02	GC	5.62	1.27
B02	NSC	2.08	0.76
B03	Isolated	24.66	–
B03	YSC	6.07	0.14
B03	GC	6.97	1.50
B03	NSC	2.15	0.79
B04	Isolated	77.75	–
B04	YSC	11.93	0.23
B04	GC	8.47	1.74
B04	NSC	2.22	0.81
C02	Isolated	5.14	–
C02	YSC	2.74	0.37
C02	GC	4.58	1.75
C02	NSC	1.50	0.66
C03	Isolated	17.53	–
C03	YSC	4.98	0.61
C03	GC	5.74	2.14
C03	NSC	1.62	0.71
C04	Isolated	60.67	–
C04	YSC	9.55	0.94
C04	GC	6.98	2.53
C04	NSC	1.72	0.76
D02	Isolated	4.41	–
D02	YSC	2.38	0.08
D02	GC	3.73	0.83
D02	NSC	1.32	0.47
D03	Isolated	13.23	–
D03	YSC	4.39	0.11
D03	GC	4.74	1.00
D03	NSC	1.43	0.51
D04	Isolated	45.85	–
D04	YSC	8.43	0.17
D04	GC	5.82	1.17
D04	NSC	1.52	0.54

Column 1: Model name; column 2: formation channel; column 3, $\mathcal{R}(0)$: merger rate density of BBHs at $z = 0$ in units of $\text{Gpc}^{-3} \text{yr}^{-1}$; column 4, $\mathcal{R}_{\text{Ng}}(0)$: merger rate density of Nth generation (Ng) BBHs with $N > 1$ at $z = 0$, in units of $\text{Gpc}^{-3} \text{yr}^{-1}$.

is the detection efficiency of the model. In eq. 25, $p_{\text{det}}(\theta)$ is the probability of detecting a source with parameters θ and can be inferred by computing the optimal signal-to-noise ratio and comparing it to a detection threshold, as described, e.g., in Bouffanais et al. (2021). The values for the event’s log-likelihood are derived from the posterior and prior samples released by the LVC, such that the integral in

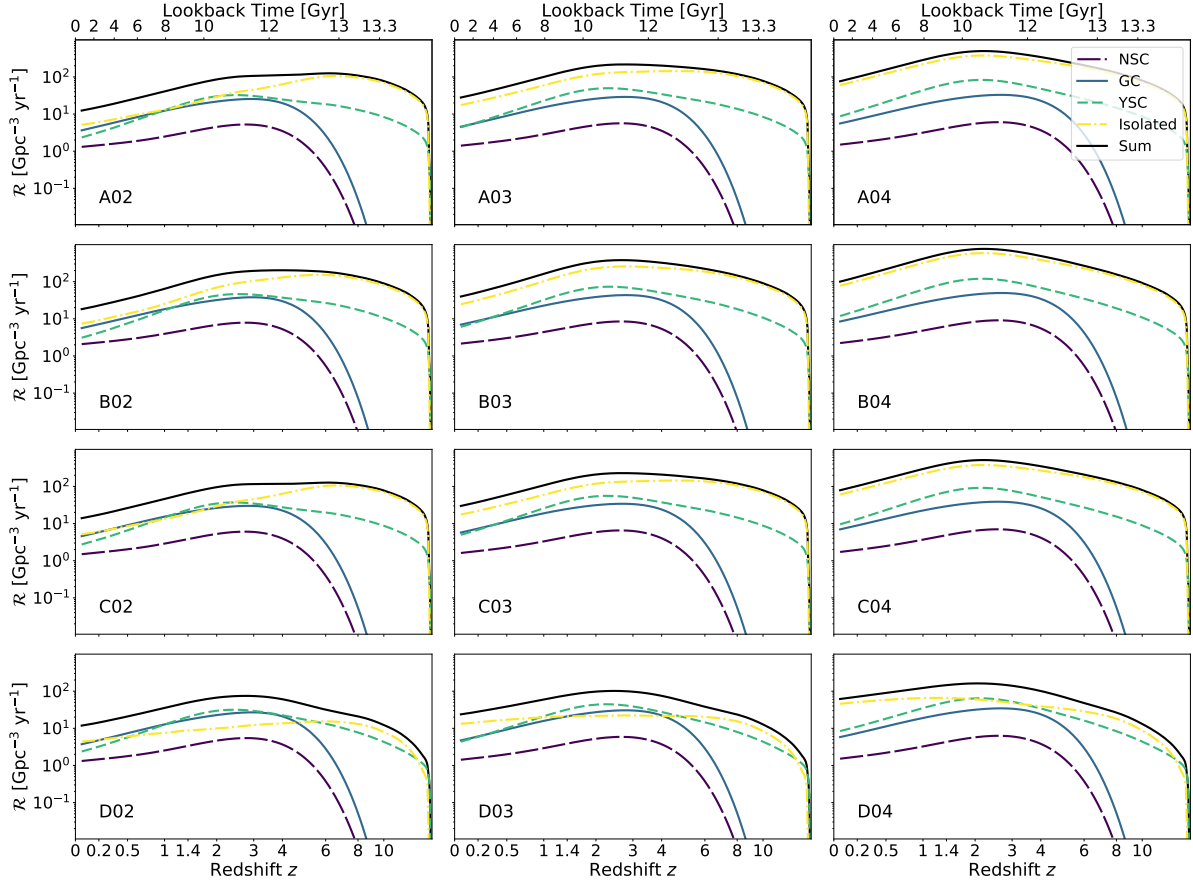


Figure 3. BBH merger rate density $\mathcal{R}(z)$ as a function of redshift, in the comoving frame, for all the models listed in Table 1. From left to right, the upper row shows models A02, A03 and A04, the second row models B02, B03 and B04, the third row models C02, C03 and C04 and the lower row models D02, D03 and D04. In all the panels, yellow dot-dashed line: isolated BBHs; light-blue short-dashed line: BBHs in YSCs; blue solid line: BBHs in GCs; dark-blue long-dashed line: BBHs in NSCs; black solid line: total merger rate density.

equation 24 is approximated with a Monte Carlo approach as

$$\mathcal{I}^k = \int_{\theta} \mathcal{L}^k(h^k|\theta) p(\theta|\lambda) d\theta \sim \frac{1}{N_s^k} \sum_{i=1}^{N_s^k} \frac{p(\theta_i^k|\lambda)}{\pi^k(\theta_i^k)}, \quad (26)$$

where θ_i^k is the i -th posterior sample for the k -th detection and N_s^k is the total number of posterior samples for the k -th detection. Both the model and prior distributions are estimated with Gaussian kernel density estimation.

In our analysis, we further marginalise eq. 24 over N_λ using a prior $\pi(N_\lambda) \sim 1/N_\lambda$ (Fishbach et al. 2018), which yields the following expression

$$p(\lambda|\mathcal{H}) \sim \pi(\lambda) \prod_{k=1}^{N_{\text{obs}}} \frac{\mathcal{I}^k}{\beta(\lambda)}, \quad (27)$$

where the integral can be approximated in the same way as in eq. 26 and $\beta(\lambda)$ is given by eq. 25. We make this choice to neglect the information coming from the number of sources predicted by the model when estimating the posterior distribution. By doing this assumption, our analysis is not affected by the large uncertainties on the rates (see, e.g., Section 4). More details on this procedure are described in Mandel et al. (2019) and Bouffanais et al. (2021).

In our analysis, our model distribution is the sum of the contributions from multiple channels (isolated BBHs, dynamical BBHs in

YSCs, GCs and NSCs) weighted by mixing fraction hyper-parameters as

$$p(\theta|f_{\text{iso}}, f_{\text{YSC}}, f_{\text{GC}}, f_{\text{NSC}}, \lambda) = f_{\text{iso}} p(\theta|\text{iso}, \lambda) + f_{\text{YSC}} p(\theta|\text{YSC}, \lambda) + f_{\text{GC}} p(\theta|\text{GC}, \lambda) + f_{\text{NSC}} p(\theta|\text{NSC}, \lambda), \quad (28)$$

where f_{iso} , f_{YSC} , f_{GC} and f_{NSC} are the mixing fractions of BBHs from isolated binary stars, YSCs, GCs and NSCs, defined so that $f_{\text{iso}} + f_{\text{YSC}} + f_{\text{GC}} + f_{\text{NSC}} = 1$. Based on this definition, the mixing fraction for each channel approximately is the fraction of merger events associated with that specific channel.

In our analysis, we do not consider all GWTC-2 event candidates (Abbott et al. 2021b) but only the 45 BBHs analyzed in Abbott et al. (2021c), which represent a sub-sample with false alarm rate $< 1 \text{ yr}^{-1}$. For these 45 BBHs, we use the GWTC-2 posterior samples for $\theta = \{\mathcal{M}, q, \chi_{\text{eff}}, z\}$, where $\mathcal{M} = (m_1 m_2)^{3/5} (m_1 + m_2)^{-1/5}$ is the chirp mass, $q = m_2/m_1$ is the mass ratio, and χ_{eff} is the effective spin:

$$\chi_{\text{eff}} = \frac{(m_1 \vec{\chi}_1 + m_2 \vec{\chi}_2) \cdot \vec{L}}{m_1 + m_2} \cdot \frac{\vec{L}}{L}, \quad (29)$$

where \vec{L} is the BBH orbital angular momentum, while $\vec{\chi}_1$ and $\vec{\chi}_2$ are the dimensionless spin vectors. We used a Metropolis-Hastings algorithm to generate samples from the posterior of eq. 27. We ran

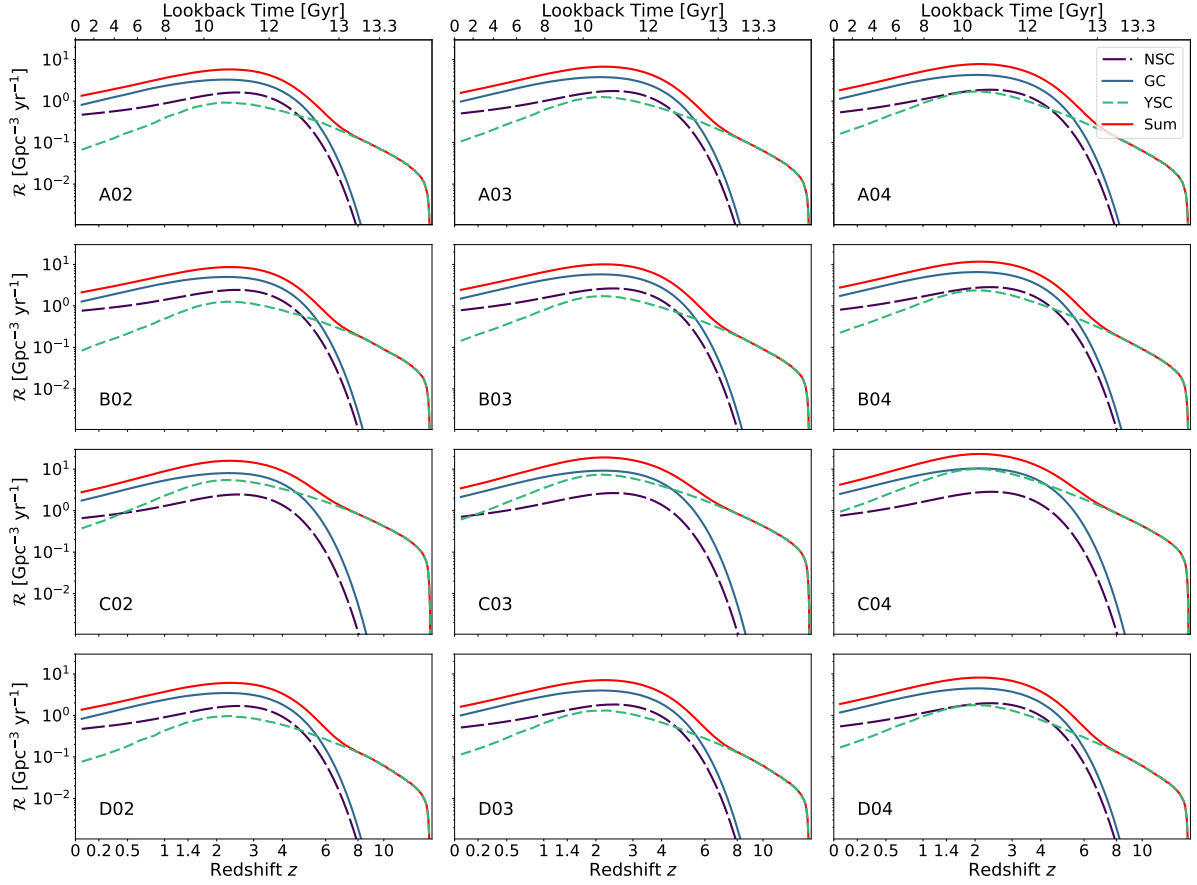


Figure 4. Merger rate density of N th generation (N_g) BBHs $\mathcal{R}_{N_g}(z)$ as a function of redshift, in the comoving frame, for all the models listed in Table 1. The order of the panels is the same as in Fig. 3. In all the panels, light-blue short-dashed line: BBHs in YSCs; blue solid line: BBHs in GCs; dark-blue long-dashed line: BBHs in NSCs; red solid line: total merger rate density of N_g BBHs.

chains of 10^7 iterations for each set of hyper-parameters, and then trimmed the chains using auto-correlation length.

3 RESULTS

3.1 Multi-channel rates

Figure 3 shows the BBH merger rate density as a function of redshift, while Table 2 shows the BBH merger rate density at $z = 0$, for all of our models. The BBH merger rate density evolution of NSCs and GCs are only weakly affected by the metallicity spread σ_Z , because BBHs efficiently pair up and harden in these massive star clusters, regardless of progenitor’s metallicity. In contrast, the merger rate density of isolated BBHs is dramatically affected by progenitor’s metallicity. As already discussed in previous work (e.g., Chruslinska et al. 2019; Santoliquido et al. 2021; Mandel & Broekgaarden 2021), there is about one order of magnitude difference in the BBH merger rate if we assume $\sigma_Z = 0.2$ or 0.4 . The behaviour of YSCs is intermediate between the field and GCs/NSCs.

The impact of the core-collapse SN model is nearly the same for all considered channels: the local BBH merger rate is $\approx 40 - 60\%$ higher if we assume the rapid instead of the delayed SN model. This happens because the minimum mass of $1g$ BHs is higher in the rapid ($m_{\min} = 5 M_{\odot}$) than in the delayed model ($m_{\min} = 3 M_{\odot}$), leading

to a shorter GW decay time. Actually, the difference between the two SN models tends to be slightly higher for GC and NSC BBHs than for isolated BBHs, because larger BH masses favour their retention inside the parent star cluster after the SN kick.

The merger rate density of isolated BBHs is $\approx 16 - 32\%$ higher if we assume $\alpha_{CE} = 1$ than if we assume $\alpha_{CE} = 5$, as already discussed by Giacobbo & Mapelli (2020). In contrast, the BBH merger rate density of YSCs, GCs and NSCs is almost unaffected by the choice of the common envelope parameter.

The merger rate density of isolated BBHs and YSC BBHs extends to higher redshift with respect to GC BBHs and NSC BBHs, but this is probably a mere effect of the extrapolation of the fitting formula for the SFR density to redshift $z \gtrsim 10$, where we do not have measurements (Madau & Fragos 2017). Furthermore, we do not model population III stars in this work (see, e.g. Ng et al. 2021 for an accurate modeling of BBHs from metal-free stars).

The total local merger rate density (i.e., the sum of the merger rate densities of the four channels) is within the 90% credible interval of the value inferred by the LVC [$\mathcal{R}(0) = 19.3^{+15}_{-9} \text{ Gpc}^{-3} \text{ yr}^{-1}$ if GW190814 is not considered a BBH and if we allow the merger rate to evolve with redshift, Abbott et al. 2021c] for the models A02, A03, B02, C02, C03, D02 and D03, while it is too high in the other models. In particular, the models with $\sigma_Z = 0.4$ (A04, B04, C04 and D04) always produce a total local merger rate $\mathcal{R} > 60 \text{ Gpc}^{-3} \text{ yr}^{-1}$,

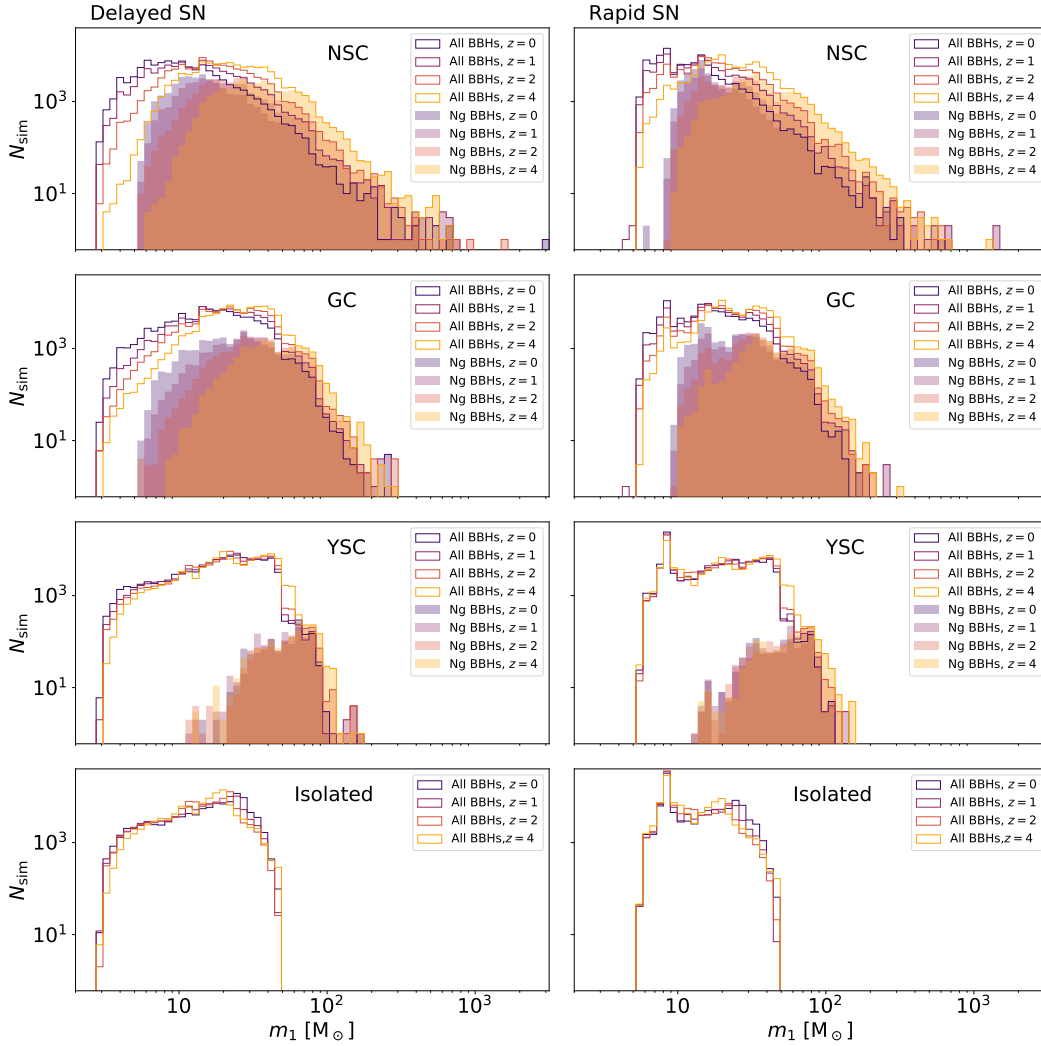


Figure 5. Distribution of primary BH masses in BBH mergers. From top to bottom: NSCs, GCs, YSCs and isolated BBHs. Left-hand column: model A03 (exploiting the delayed SN model); right-hand column: model B03 (with the rapid SN model). Unfilled histograms: all BBH mergers; filled histograms: Ng BBH mergers (with $N > 1$). Blue, purple, pink and orange histograms: BBHs merging at $z = 0, 1, 2$ and 4 , respectively. We show the same number of simulated BBHs per each channel and per each redshift.

which is a factor of > 3 higher than the median value inferred by the LVC.

Figure 4 shows the merger rate density evolution of Ng BHs only, with $N > 1$. The fourth column of Table 2 reports the local merger rate density of Ng BBHs. GCs give the main contribution to the merger rate of Ng BBHs in all our models [$\mathcal{R}_{\text{Ng}}(0) \approx 0.8 - 2.5 \text{ Gpc}^{-3} \text{ yr}^{-1}$], followed by NSCs [$\mathcal{R}_{\text{Ng}}(0) \approx 0.5 - 1 \text{ Gpc}^{-3} \text{ yr}^{-1}$] and YSCs [$\mathcal{R}_{\text{Ng}}(0) \approx 0.1 - 0.9 \text{ Gpc}^{-3} \text{ yr}^{-1}$]. In models A02–A04, the merger rate of Ng BHs is $\approx 36\%$, $\approx 22\%$ and $\approx 2 - 3\%$ of the total merger rate in NSCs, GCs and YSCs, respectively.

Models C02–C04 have higher values of \mathcal{R}_{Ng} with respect to the other models, because lower spin magnitudes are associated with lower relativistic kicks and hence favour the merger of Ng BHs. The spin magnitude parameter σ_χ has a stronger impact on the rate of Ng BBH mergers in YSCs than in GCs and especially NSCs. For example, the local Ng BBH rate in YSCs is a factor of ≈ 6 higher in model C03 ($\sigma_\chi = 0.01$) with respect to model A03 ($\sigma_\chi = 0.1$). In the case of GCs and NSCs, the difference between the C03 and

A03 models is equal to a factor of ≈ 2 and ≈ 1.4 , respectively. This trend is a consequence of the different escape velocities of YSCs, GCs and NSCs: in our models, NSCs have escape velocities of the order of 100 km s^{-1} , hence they retain a large fraction of the merger remnants even if $\sigma_\chi = 0.1$; in contrast, GCs and especially YSCs have lower escape velocities and lose most of their BH merger remnants if $\sigma_\chi = 0.1$. If we lower σ_χ to 0.01, even YSCs can efficiently retain their BH merger remnants. Accounting for all these uncertainties, the total merger rate of Ng BBHs in the local Universe ranges from $\approx 1 \text{ Gpc}^{-3} \text{ yr}^{-1}$ (D02) to $\approx 4 \text{ Gpc}^{-3} \text{ yr}^{-1}$ (C04).

3.2 BBH mass

Figure 5 shows the distribution of the primary BH masses in the four considered channels at different redshifts, for models A03 (delayed SN model) and B03 (rapid SN model). The overall primary BH mass distribution strongly depends on the core-collapse SN model by construction: while the delayed SN model allows the formation

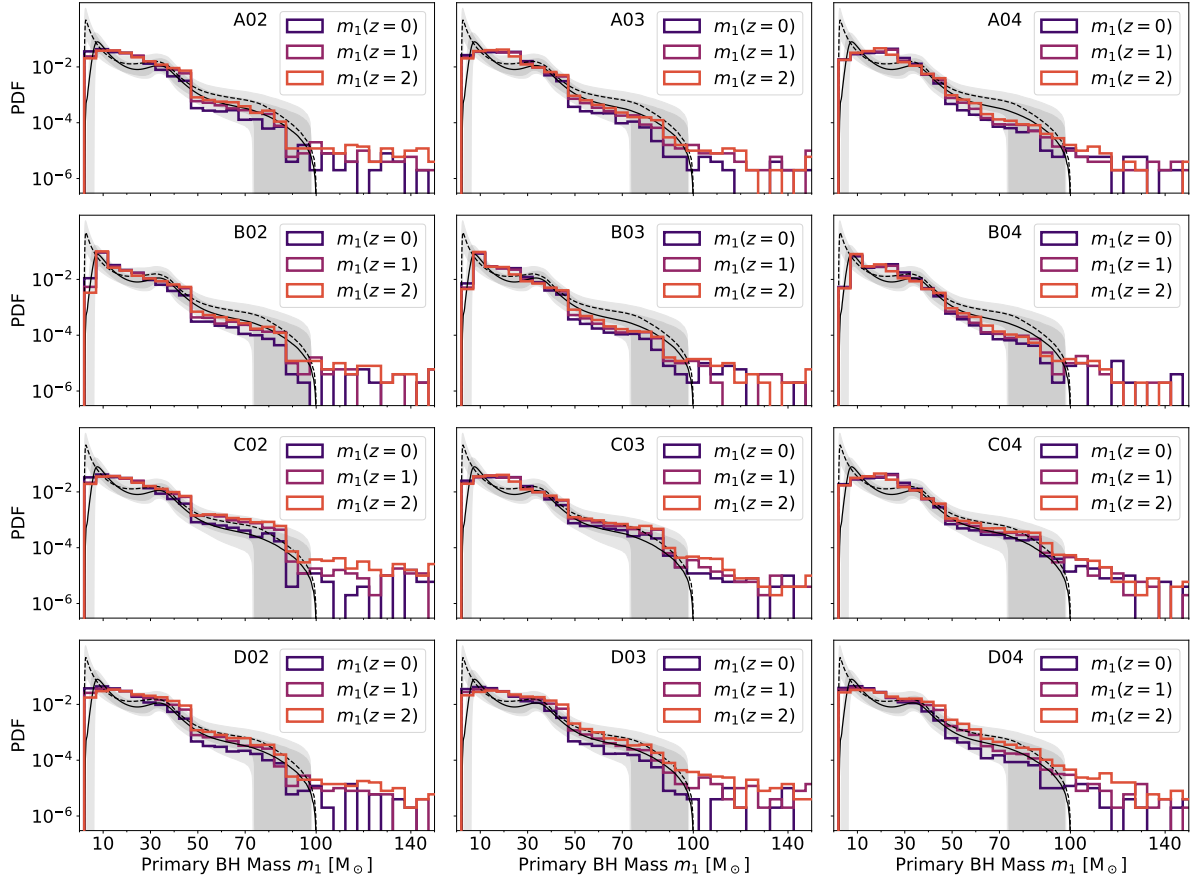


Figure 6. Probability distribution function of primary BH masses (m_1) of BBHs merging at redshift $z = 0$ (blue), $z = 1$ (purple) and $z = 2$ (pink). In each panel, we have put together different channels (isolated, YSC, GC and NSC) based on their merger rate, to obtain a synthetic Universe. We truncate the plots at $150 M_\odot$ to improve the readability of this Figure, but there are several BHs with even higher masses (see Fig. 5). The order of the panels is the same as in Fig. 3. The black solid (dashed) line is the median value of the POWER LAW + PEAK model applied to GWTC-2 BBHs excluding (including) GW190814 (Abbott et al. 2021c). The shaded gray areas are the corresponding 90% credible intervals. We arbitrarily rescaled the POWER LAW + PEAK model on the y axis.

of BHs with mass as low as $3 M_\odot$, the rapid SN model prevents the formation of BHs with mass $< 5 M_\odot$.

The mass function of primary BHs in YSCs is similar to the distribution of primary BHs in isolated binary systems, but while the latter has a sharp truncation at $\approx 50 M_\odot$, the former has a tail up to $\approx 200 M_\odot$ because of Ng systems.

The contribution of dynamically formed BBHs and Ng BBHs is more important for NSCs and GCs, which are the most dynamically active systems. However, BHs with mass $> 100 M_\odot$ are extremely rare even in GCs and NSCs. As already discussed in Mapelli et al. (2021), NSCs are the channel with the largest number of low-mass primary BHs. This happens because single BHs that receive a SN kick higher than the escape velocity leave their parent star cluster and cannot pair up dynamically. Since the natal kick in our models is higher for less massive BHs, this strongly suppresses the formation of light BBHs in YSCs and GCs, which have relatively low escape velocity, while NSCs are able to retain even the least massive BHs.

The mass distribution of isolated BBHs and YSC BBHs does not show any strong dependence on the merger redshift. In contrast, the mass distribution of BBHs in GCs and especially NSCs shows a relevant trend: low-mass BBH mergers are more common at low redshift than at high redshift. This is a consequence of dynamics: more massive BHs dynamically pair up on a shorter timescale than

lighter BHs (eq. 1). Moreover, the timescale for GW decay is shorter for more massive systems than for lighter ones (eqs. 5).

Figure 6 shows a realization of the primary BH mass distribution we obtain by putting together BBHs from various channels according to their merger rate. In other words, this is the entire population of BBH mergers at $z = 0, 1$ and 2 in our synthetic Universe, without including observation biases. The most notable difference is between the rapid and delayed model, the former displaying a stronger peak at primary mass $m_1 \approx 10 M_\odot$ with respect to the latter. The tail of high-mass BHs ($\geq 50 M_\odot$) is more populated in models C02–C04 with respect to the other models, because the low-spin models have a higher percentage of Ng BBHs.

Going from models with $\sigma_Z = 0.2$ to models with $\sigma_Z = 0.4$, the contribution of primary BHs with mass $m_{\text{BH}} \sim 20 M_\odot$ becomes more and more important, because the isolated BBH channel (which has the largest population of BHs with mass $m_{\text{BH}} \sim 20 M_\odot$, Fig. 5) is associated with a higher merger rate for larger values of σ_Z .

In Figure 6, we also visually compare our synthetic populations with the POWER LAW + PEAK model from Fig. 8 of Abbott et al. (2021c). Our populations match the POWER LAW + PEAK model, the main difference being the number of primary BHs with mass $\sim 20 M_\odot$, which is higher in our models, especially if we adopt the delayed model and $\sigma_Z = 0.4$. At the high-mass end, our low spin

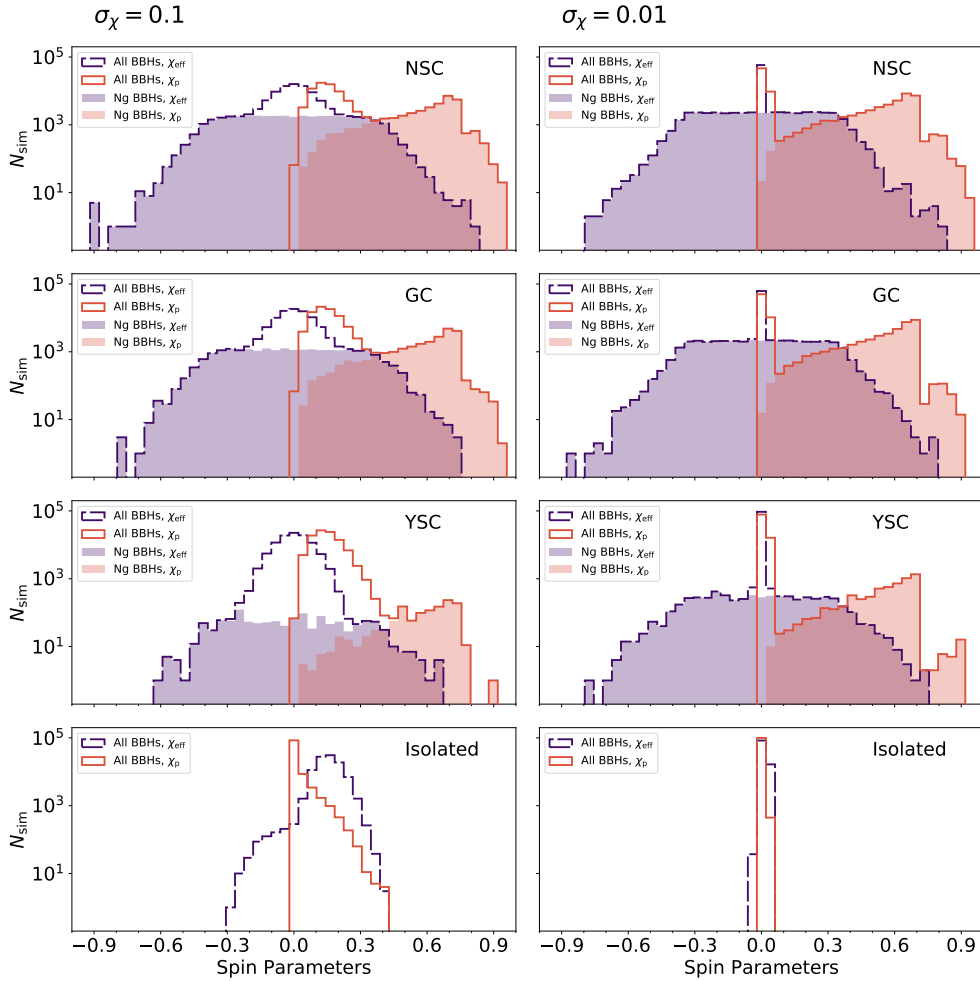


Figure 7. Distribution of effective spins (χ_{eff} , blue) and precessing spins (χ_p , red) in BBH mergers at redshift $z = 0$. From top to bottom: NSCs, GCs, YSCs and isolated BBHs. Left-hand column: model A03 ($\sigma_\chi = 0.1$); right-hand column: model C03 ($\sigma_\chi = 0.01$). Unfilled histograms: all BBH mergers; filled histograms: Ng BBH mergers (with $N > 1$). We show the same number of simulated BBHs per each channel.

models C02–C04 better match the POWER LAW + PEAK model than the other runs, but all of our synthetic populations are within the 90% credible interval of the phenomenological model by Abbott et al. (2021c).

Figure 6 compares the population of BBHs at redshift 0, 1 and 2. The fraction of BBHs with primary mass $\geq 30 M_\odot$ increases with redshift, because of the contribution of GCs and NSCs to the overall BBH population (Fig. 5). This dependence on redshift is more evident in models with $\sigma_z = 0.2$ and $\alpha = 5$, in which the contribution of isolated BBHs is quenched. From GWTC-2 data, there is no clear evidence that the mass of BBH mergers evolves with redshift (Abbott et al. 2021b,c), but some recent analysis suggests a possible weak trend under several assumptions (Fishbach et al. 2021; Fishbach & Kalogera 2021). In our models, we also predict a weak trend, driven by BBHs in GCs and NSCs.

3.3 BBH spins

Figure 7 shows the distribution of effective (χ_{eff} , eq. 29) and precessing spins (χ_p) for our BBH mergers at redshift $z = 0$. We calculated

χ_p according to the following definition:

$$\chi_p = \max \left[\chi_{1\perp}, \frac{q(4q+3)}{4+3q} \chi_{2\perp} \right], \quad (30)$$

where $\chi_{1\perp}$ and $\chi_{2\perp}$ are the components of the dimensionless spin vectors ($\vec{\chi}_1$ and $\vec{\chi}_2$) perpendicular to the orbital angular momentum.

The distribution of χ_{eff} and χ_p is nearly independent of redshift, but this is not surprising, because we derive the magnitudes of 1g BBHs from a toy model which does not depend on either redshift or mass. In the dynamical channels χ_{eff} is symmetric around zero, because we assume isotropic spin orientation, while the isolated channel has a strong preference for positive χ_{eff} because of angular momentum alignment during mass transfer and tidal evolution. Ng mergers extend the distribution of χ_{eff} to very low and very high values with respect to 1g mergers.

The distribution of χ_p for isolated BBHs has a strong peak at zero, because of the preferential alignment, while the distribution of χ_p for dynamical BBHs has two peaks. The position of the primary peak depends on the choice of σ_χ , while the secondary peak is at $\chi_p \approx 0.7$ and is completely determined by Ng BBHs.

Fig. 8 shows the distribution of χ_{eff} and χ_p we obtain by putting to-

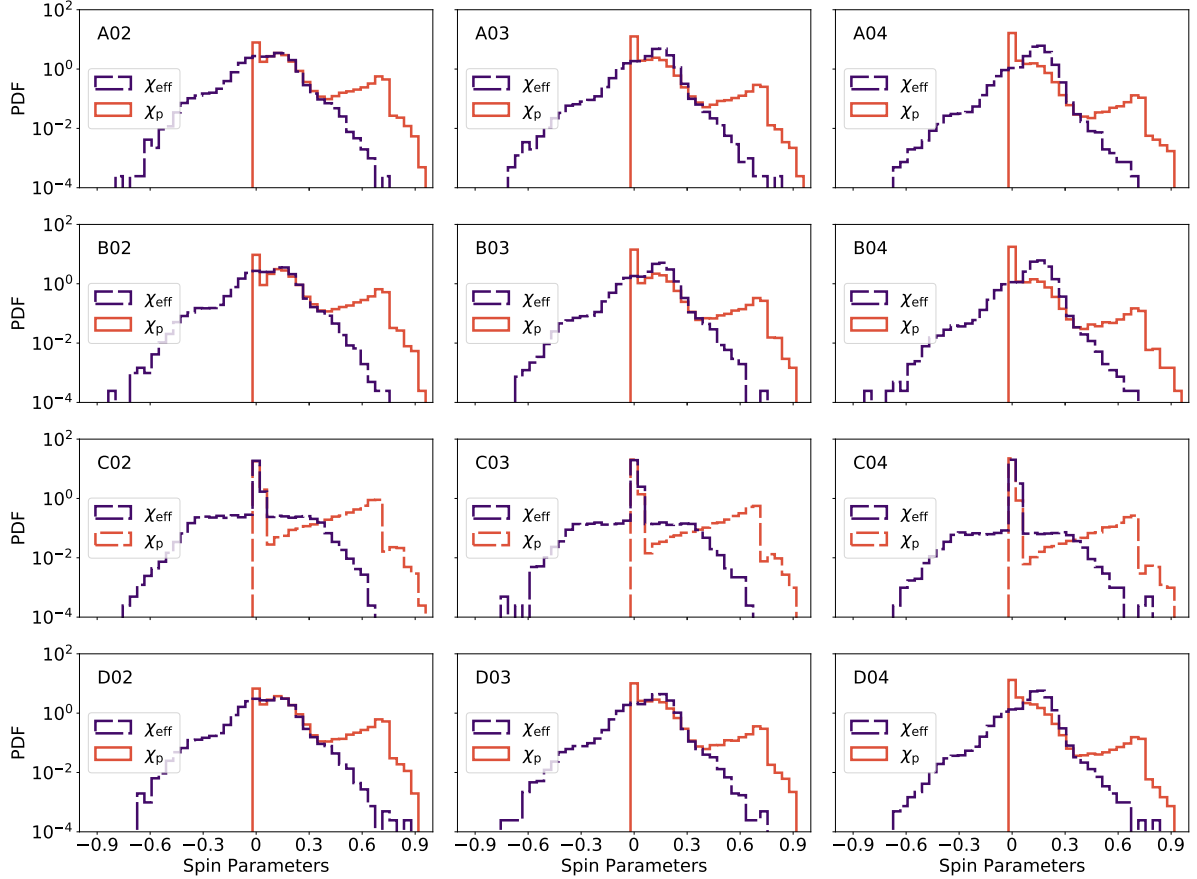


Figure 8. Probability distribution function of effective (χ_{eff} , blue dashed line) and precessing spin (χ_p , red solid line) of BBHs merging at $z = 0$. In each panel, we have put together different channels (isolated, YSC, GC and NSC) based on their merger rate, to obtain a synthetic Universe, as already done in Fig. 6. The order of the panels is the same as in Fig. 3.

gether BBHs formed via different channels according to their merger rate at $z = 0$. In the fiducial spin case ($\sigma_\chi = 0.1$), the distribution of χ_{eff} becomes more asymmetric if we assume a larger value of σ_Z , because the contribution of isolated BBHs to the total merger population increases for larger metallicity spreads. In the low-spin case ($\sigma_\chi = 0.01$), this dependence on σ_Z is not visible because all 1g BBHs have vanishingly small spins.

In the fiducial spin case ($\sigma_\chi = 0.1$), the total distribution of χ_p even shows three peaks: a first narrow peak at zero because of isolated BBHs, a second broader peak at $\chi_p \sim 0.1 - 0.2$ because of 1g dynamical BBHs and a third peak at $\chi_p \sim 0.7$ because of Ng mergers. The peak at $\chi_p \sim 0.1 - 0.2$ is an effect of our choice of σ_χ . In the low-spin case ($\sigma_\chi = 0.01$) there are only two peaks: one at zero (due to both isolated BBHs and 1g dynamical BBHs) and the other at 0.7 (Ng BBHs).

3.4 Mixing fractions

Figure 9 shows the posterior distribution of the mixing fractions f_i (with $i = \text{iso, YSC, GC and NSC}$), defined in eq. 28. These values are obtained taking into account the detection efficiency (eq. 25) and marginalizing eq. 26 over N_λ (eq. 27). Table 3 shows the median and 90% credible interval of the mixing fractions. The mixing fractions wildly depend on the details of each model: small differences between one model and another result in large differences in terms of f_i . There

are still too many uncertainties about astrophysical models to claim we know the relative impact of each channel onto the global merger population.

However, there is a common feature of all our models: GWTC-2 data moderately support the co-existence of multiple channels: in each of our models, the mixing fraction is significantly larger than zero for at least two of the four considered channels. Hence, multiple formation channels likely are at work, to produce the population of BBH mergers we observe with GWs. In particular, the contribution of either isolated BBHs or BBHs in YSCs is needed to explain the low-mass portion of the BH mass function (Figs. 5 and 6), while the contribution of BBHs in GCs or NSCs is fundamental to reproduce the high-mass tail ($m_1 \geq 50 M_\odot$).

Isolated BBHs are associated with higher mixing fractions in models with very low spins (C02–C04) possibly because the observed population does not favour a strongly asymmetric χ_{eff} distribution with support for large positive values (Abbott et al. 2021c).

The metallicity spread also has a large effect on the mixing fractions. Fig. 9 does not account for the predicted number of detections. Hence, the impact of σ_Z on our mixing fractions is rather connected with BH mass and redshift distribution than with rates. A larger metallicity spread increases the percentage of isolated BBHs born from metal-poor stars that merge in the low-redshift Universe. Since these tend to be more massive than BBHs from metal-rich stars, the mass function of isolated BBHs tends to be more top-heavy when

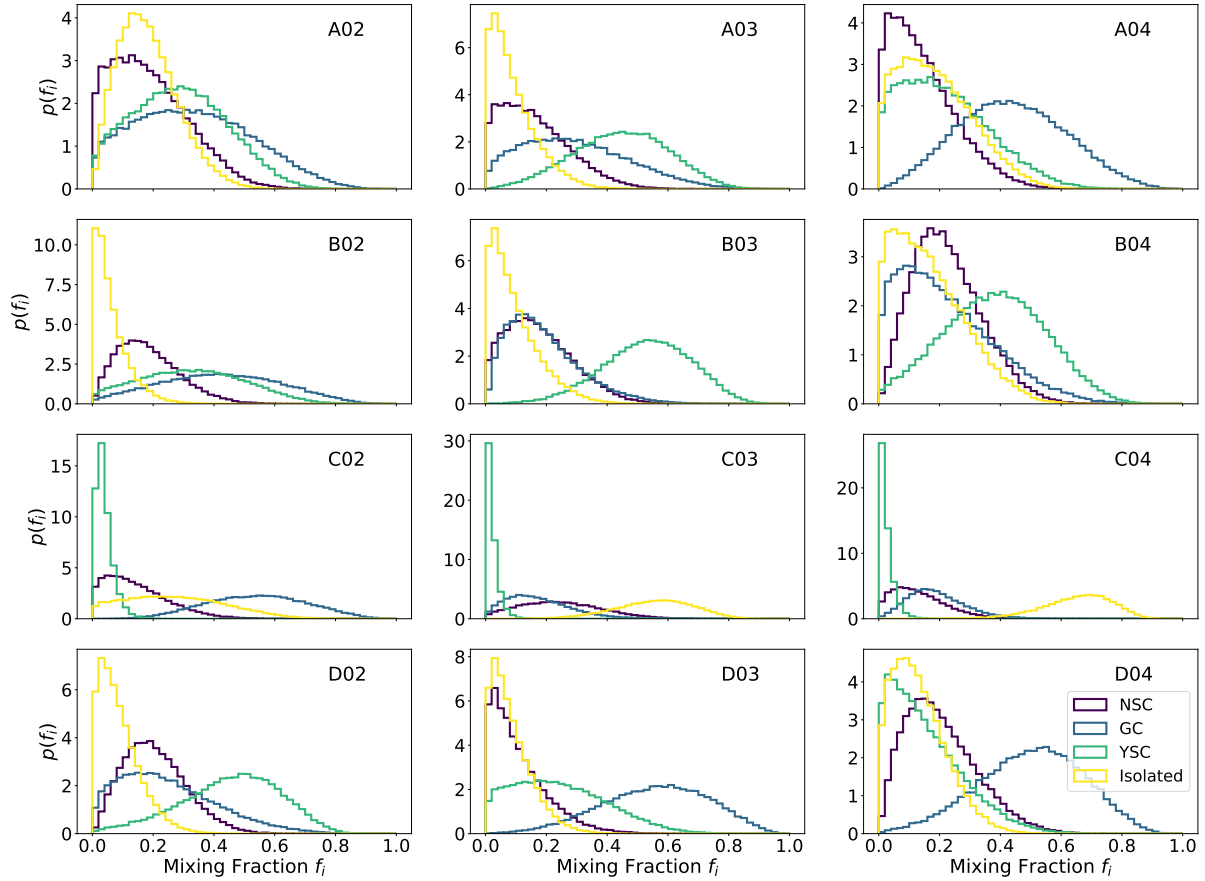


Figure 9. Posterior probability distribution of the mixing fractions f_i (with $i = \text{iso, YSC, GC and NSC}$, eq. 28) for all our models. The order of the panels is the same as in Fig. 3. Yellow dot-dashed line: isolated BBHs; light-blue short-dashed line: BBHs in YSCs; blue solid line: BBHs in GCs; dark-blue long-dashed line: BBHs in NSCs. To produce this Figure we used the posterior samples from GWTC-2 (Abbott et al. 2021b).

σ_Z is large, hence more similar to the one of dynamical BBHs. As a consequence, f_{iso} tends to be larger.

Figure 10 shows the values of \mathcal{I}^k (defined in eq. 26) for model A03. The other models yield similar results. The integral \mathcal{I}^k gives an idea of how well our models are able to match the posterior distributions of a GW event. Figure 10 only shows the 10 BBHs with the largest chirp mass from GWTC-2 (Abbott et al. 2021b). The isolated channel struggles to explain the five most massive events, which have $M \geq 40 M_\odot$. In the case of GW190521, we find $\ln(\mathcal{I}^k) \approx -453$, even if we do not include χ_p among the considered parameters. While a strongly negative value of \mathcal{I}^k for a single event does not significantly affect the mixing fractions, significantly negative values for at least five BBHs (over the 45 events we included in our sample) have some impact on f_i . In model A03, the mixing fraction of the isolated channel increases from $f_{\text{iso}} = 0.07^{+0.17}_{-0.07}$ to $0.10^{+0.20}_{-0.09}$ if we recalculate it after removing the five events with the largest chirp mass (the reported uncertainty is the 90% credible interval). Correspondingly, the mixing fraction of GCs decreases from $f_{\text{GC}} = 0.28^{+0.33}_{-0.23}$ to $0.21^{+0.32}_{-0.18}$ when we remove these five events, while f_{YSC} and f_{NSC} remain nearly unchanged.

Table 3. Median values of the mixing fractions.

Model	f_{iso}	f_{YSC}	f_{GC}	f_{NSC}
A02	$0.17^{+0.19}_{-0.13}$	$0.28^{+0.26}_{-0.23}$	$0.32^{+0.34}_{-0.27}$	$0.17^{+0.25}_{-0.15}$
A03	$0.07^{+0.17}_{-0.07}$	$0.45^{+0.25}_{-0.27}$	$0.28^{+0.33}_{-0.23}$	$0.15^{+0.23}_{-0.13}$
A04	$0.17^{+0.24}_{-0.15}$	$0.20^{+0.29}_{-0.18}$	$0.43^{+0.30}_{-0.28}$	$0.13^{+0.23}_{-0.11}$
B02	$0.05^{+0.13}_{-0.04}$	$0.33^{+0.29}_{-0.27}$	$0.42^{+0.32}_{-0.32}$	$0.17^{+0.20}_{-0.13}$
B03	$0.08^{+0.18}_{-0.07}$	$0.54^{+0.22}_{-0.26}$	$0.17^{+0.26}_{-0.13}$	$0.16^{+0.22}_{-0.14}$
B04	$0.15^{+0.24}_{-0.13}$	$0.38^{+0.27}_{-0.28}$	$0.19^{+0.33}_{-0.17}$	$0.21^{+0.22}_{-0.15}$
C02	$0.26^{+0.30}_{-0.23}$	$0.03^{+0.06}_{-0.03}$	$0.54^{+0.26}_{-0.27}$	$0.13^{+0.22}_{-0.11}$
C03	$0.56^{+0.19}_{-0.23}$	$0.02^{+0.04}_{-0.01}$	$0.16^{+0.21}_{-0.13}$	$0.24^{+0.24}_{-0.19}$
C04	$0.66^{+0.15}_{-0.22}$	$0.02^{+0.05}_{-0.02}$	$0.18^{+0.19}_{-0.12}$	$0.12^{+0.18}_{-0.10}$
D02	$0.08^{+0.15}_{-0.07}$	$0.47^{+0.23}_{-0.29}$	$0.23^{+0.33}_{-0.31}$	$0.20^{+0.20}_{-0.14}$
D03	$0.07^{+0.15}_{-0.06}$	$0.23^{+0.29}_{-0.20}$	$0.57^{+0.26}_{-0.31}$	$0.09^{+0.21}_{-0.08}$
D04	$0.12^{+0.18}_{-0.10}$	$0.13^{+0.26}_{-0.12}$	$0.51^{+0.26}_{-0.31}$	$0.19^{+0.24}_{-0.14}$

This Table shows the median values and 90% intervals of the mixing fractions shown in Fig. 9.

4 DISCUSSION: MAIN SOURCES OF UNCERTAINTY AND FURTHER CAVEATS

The formation rate density of star clusters is extremely uncertain. Here, we discuss what happens if we consider different assumptions within the observational uncertainties. For GCs, we start from model A03 and change the normalization \mathcal{B}_{GC} , the position of the peak z_{GC}

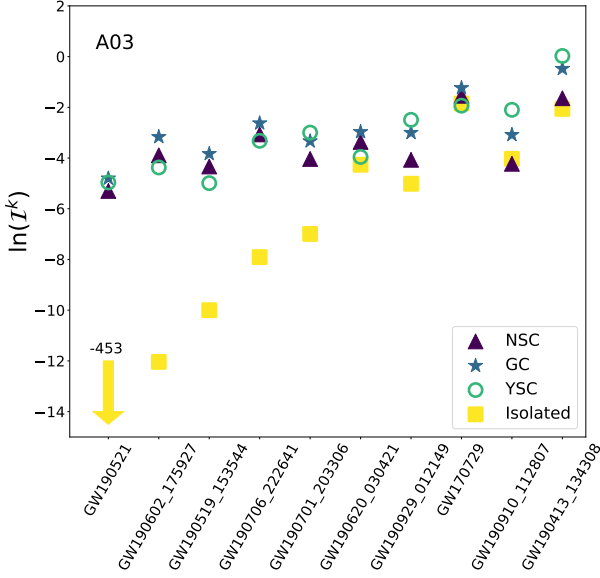


Figure 10. Value of I^k (eq. 26) for the 10 GWTC-2 events with the largest chirp mass M . The GW events on the x axis are ordered by decreasing median value of M . Yellow squares: isolated BBHs; light-blue open circles: BBHs in YSCs; blue stars: BBHs in GCs; dark-blue triangles: BBHs in NSCs.

and the spread of the distribution σ_{GC} . A change of the normalization of the GC formation rate causes the same change of the value of the BBH merger rate density: if we increase (reduce) the normalization by a factor of two from $\mathcal{B}_{GC} = 2 \times 10^{-4}$ to 4×10^{-4} (10^{-4}) $M_{\odot} \text{Mpc}^{-3} \text{yr}^{-2}$, we obtain a factor of two higher (lower) merger rate density at each redshift, as shown in Fig. 11.

If we change the peak redshift from $z_{GC} = 3.2$, as inferred from Galactic GCs, to $z_{GC} = 4$, as suggested by the models of [El-Badry et al. \(2019\)](#), the BBH merger rate density also shifts: the maximum value of $\mathcal{R}(z)$ is at redshift $z = 3.55$ ($z = 2.75$) when $z_{GC} = 4$ ($z_{GC} = 3.2$). This shift of the peak has a strong impact on the local merger rate density, which decreases from $\mathcal{R}(0) \approx 5 \text{Gpc}^{-3} \text{yr}^{-1}$ to $\mathcal{R}(0) \approx 2 \text{Gpc}^{-3} \text{yr}^{-1}$ if we change z_{GC} from 3.2 to 4. Finally, the standard deviation σ_{GC} has an even larger impact on the local merger rate: $\mathcal{R}(0)$ drops from $\approx 5 \text{Gpc}^{-3} \text{yr}^{-1}$ to $\approx 0.3 \text{Gpc}^{-3} \text{yr}^{-1}$ if we change σ_{GC} from 1.5 to 0.5. However, $\sigma_{GC} = 0.5$ is an extreme value when compared with other models (e.g., [El-Badry et al. 2019](#); [Reina-Campos et al. 2019](#)).

The formation history of NSCs is even more uncertain. We assumed that $\psi_{NSC}(z)$ is a Gaussian function for analogy with GCs, but the shape of NSC formation history is essentially unconstrained ([Neumayer et al. 2020](#)). In Figure 12, we assume that $\psi_{NSC}(z)$ scales with the global star formation rate density $\psi(z)$ ([Madau & Fragos 2017](#)) as $\psi_{NSC}(z) = \mathcal{B}_{NSC} \psi(z)$, where $\mathcal{B}_{NSC} = 10^{-5}$, 10^{-4} and 10^{-3} in the three cases shown in Fig. 12. The case with $\mathcal{B}_{NSC} = 10^{-4}$ has a similar behaviour to our fiducial model A03 at redshift $z < 2$. The models with $\mathcal{B}_{NSC} = 10^{-3}$ and $\mathcal{B}_{NSC} = 10^{-5}$ give a local merger rate density a factor of 10 higher and a factor of 10 lower than model A03, respectively. The case with $\mathcal{B}_{NSC} = 10^{-3}$ is a strong upper limit, because it gives a local density of NSCs $n_{NSC} \sim 0.6 \text{Mpc}^{-3}$, i.e. larger than the number of galaxies which can host such NSCs.

In the case of YSCs, the main uncertainty concerns which fraction of the cosmic star formation rate happens in YSCs versus the field. In our fiducial model, we adopted a conservative assumption that only $\sim 10\%$ of the cosmic star formation rate happens in YSCs, as

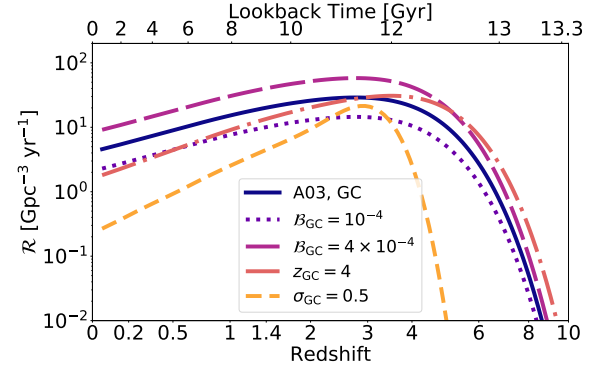


Figure 11. Merger rate density of BBHs in GCs, as a function of redshift. Different lines show the uncertainties connected with the formation rate history of GCs. Blue solid line: model A03 for GCs. Violet dotted line: same as A03 but with normalization $\mathcal{B}_{GC} = 10^{-4}$ in units of $M_{\odot} \text{Mpc}^{-3} \text{yr}^{-1}$. Magenta long-dashed line: same as A03 but with normalization $\mathcal{B}_{GC} = 4 \times 10^{-4} M_{\odot} \text{Mpc}^{-3} \text{yr}^{-1}$. Pink dash-dotted line: same as A03 but with peak redshift $z_{GC} = 4$. Orange short-dashed line: same as A03 but with standard deviation $\sigma_{GC} = 0.5$.

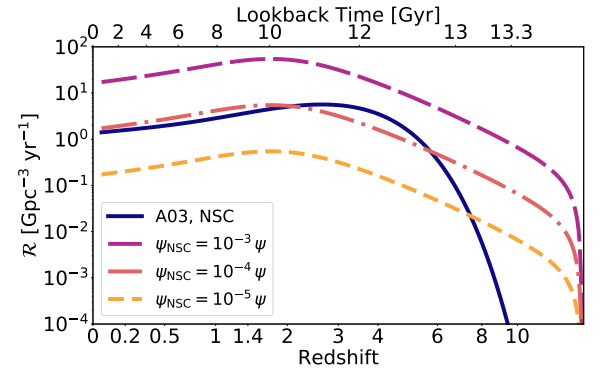


Figure 12. Merger rate density of BBHs in NSCs, as a function of redshift. Different lines show the uncertainties connected with the formation rate history of NSCs. Blue solid line: model A03 for GCs. Magenta long-dashed line: same as A03 but with NSC formation rate density $\psi_{NSC}(z) = 10^{-3} \psi(z)$ ($\psi(z)$ is defined in eq. 14). Pink dash-dotted line: same as A03 but with $\psi_{NSC}(z) = 10^{-4} \psi(z)$. Orange short-dashed line: same as A03 but with standard deviation but with $\psi_{NSC}(z) = 10^{-5} \psi(z)$.

suggested by recent studies (e.g., [Kruijssen 2014](#); [Ward et al. 2020](#)). In Figure 13, we consider two more optimistic assumptions in which $\sim 30\%$ and $\sim 70\%$ of the cosmic star formation rate happen in YSCs ([Lada & Lada 2003](#); [Portegies Zwart et al. 2010](#)). As expected, the merger rate density of BBHs in YSCs scales accordingly, while the merger rate density of isolated BBHs decreases by the corresponding amount.

Another source of uncertainty is the fraction of original versus dynamical BBHs. While the fraction of original BBHs is deemed to be very low in both GCs and NSCs (hence their population properties are mostly driven by dynamical BBHs, [Antonini & Rasio 2016](#); [Rodriguez et al. 2016](#)), the percentage of original BBHs in YSCs is more uncertain. Here, we have assumed they are 60% of all BBH mergers, based on the results of [Rastello et al. \(2021\)](#). However, [Rastello et al. \(2021\)](#) also show that the percentage of original BBHs

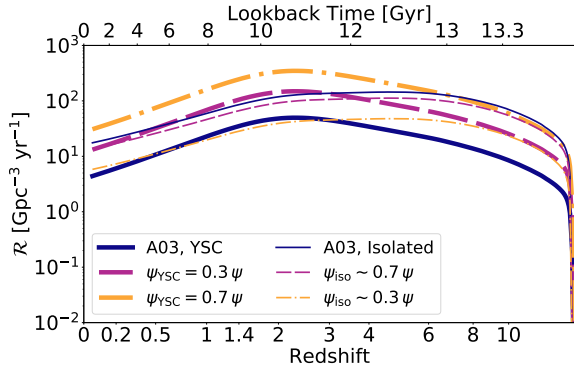


Figure 13. Merger rate density of BBHs in YSCs (thick lines) and in the field (thin lines), as a function of redshift. Different lines show the uncertainties connected with the formation rate history of YSCs. Blue thick (thin) solid line: model A03 for GCs (isolated BBHs). Magenta long-dashed line: same as A03 but with YSC formation rate density $\psi_{\text{YSC}}(z) = 0.3 \psi(z)$. Orange dash-dotted line: same as A03 but with $\psi_{\text{YSC}}(z) = 0.7 \psi(z)$.

strongly fluctuates from a cluster to another and possibly depends on both YSC mass and metallicity. Figure 14 shows the merger efficiency in the field and in YSCs (defined in eqs. 18 and 19). The merger efficiency of original BBHs in YSCs is very similar to the one of isolated BBHs, while the merger efficiency of dynamical BBHs in YSCs has a much less steep dependence on metallicity. Hence, if we assume a higher percentage of dynamical BBHs in YSCs, we end up with a higher local merger rate density in YSCs and with a milder dependence of the YSC merger rate on metallicity spread.

One of the main approximations of our approach is that we do not model stellar and binary evolution together with dynamics. This approximation is well motivated for GCs and NSCs, which have two-body relaxation timescales of several Gyrs (Binney & Tremaine 1987), but is less good for YSCs, which have two-body relaxation timescales of several ten Myrs. Di Carlo et al. (2020b) showed that most dynamical exchanges leading to the formation of merging BBHs involve their stellar progenitors, before they collapse to BHs. Moreover, hierarchical BBH mergers are rare in YSCs, but runaway collisions seem to be more efficient in producing massive BHs in these environments (Mapelli 2016; Rizzuto et al. 2021; Di Carlo et al. 2021). Thus, our results likely underestimate the presence of massive BBHs ($m_1 + m_2 > 100 M_\odot$) in YSCs. We will include a treatment of stellar/binary evolution in FASTCLUSTER in future work.

The properties of our star clusters do not evolve with time. On the one hand, star clusters lose mass by stellar evolution and dynamical ejection and expand by two-body relaxation. This leads to lower star cluster mass and density, possibly quenching the formation of hierarchical mergers (e.g., Antonini & Gieles 2020b,a). On the other hand, by assuming no evolution with time, we do not account for core collapse episodes and gravothermal oscillations, which lead to a dramatic temporary increase of the central density, possibly boosting BBH formation and hierarchical mergers (e.g., Breen & Heggie 2013). NSCs might even acquire mass during their life by fresh star formation (e.g., Mapelli et al. 2012) and by accreting GCs (e.g., Capuzzo-Dolcetta & Mocchi 2008; Antonini et al. 2012). These processes might lead to a higher efficiency of hierarchical mergers in NSCs. The overall effect of including star cluster evolution in our model is thus quite difficult to predict and might be significantly different for YSCs, GCs and NSCs. We will add a formalism for star

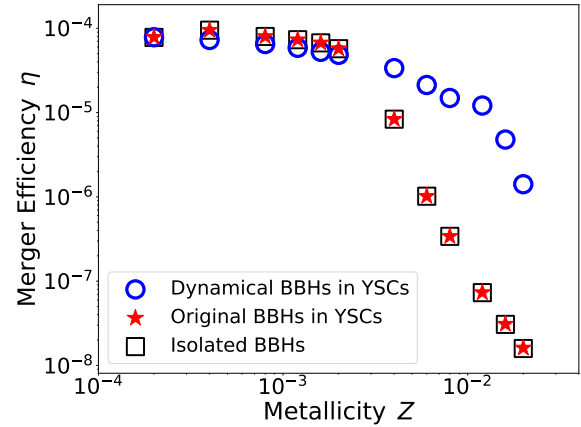


Figure 14. Merger efficiency η of BBHs as a function of metallicity Z , in model A03. Blue open circles: dynamical BBHs in YSCs. Red stars: original BBHs in YSCs. Black open squares: isolated BBHs.

cluster evolution in a follow-up study. Furthermore, we neglect the impact of additional formation channels, such as BBHs in AGN discs and field triples. The approach of FASTCLUSTER is very flexible, and we can add more channels in the future.

Comparing to previous studies, which use more sophisticated and computationally expensive simulations, we find similar results. For example, our local merger rate density in GCs is consistent with the one found by Rodriguez & Loeb (2018), even if our values [$\mathcal{R}(0) \approx 4 - 8 \text{ Gpc}^{-3} \text{ yr}^{-1}$] are rather on the lower side of their range [$\mathcal{R}(0) \approx 4 - 18 \text{ Gpc}^{-3} \text{ yr}^{-1}$]. The difference is easily explained by the fact that we do not model GW captures, which require direct N-body integration with post-Newtonian terms (Samsing 2018; Zevin et al. 2019; Kremer et al. 2020a). Moreover, we use a different mass function and spin distribution. To confirm the good performance of FASTCLUSTER, we also find that the maximum merger rate density (at $z \sim 2.8$) is about six times higher than the local merger rate density, in perfect agreement with Rodriguez & Loeb (2018). Finally, our percentages of Ng to 1g BBH mergers in GCs are comparable to the ones derived by several authors with different approaches (Rodriguez et al. 2019; Zevin et al. 2019; Kimball et al. 2021, 2020; Doctor et al. 2020). For more details on this comparison, see the Discussion in Mapelli et al. (2021).

The main result of our mixing fraction analysis is that at least two formation channels need to be at work to produce the population of GWTC-2. This result is in agreement with previous work (Abbott et al. 2021c; Zevin et al. 2021; Bouffanais et al. 2021; Wong et al. 2021). Taking advantage of FASTCLUSTER flexibility and speed, we probed a larger parameter space than previously done (including different metallicity spreads, different core-collapse SN models and a large number of stellar metallicities). This analysis shows that the mixing fraction of each channel varies wildly from one model to another, being extremely sensitive to the metallicity spread σ_Z , spin parameter σ_χ , common envelope parameter and core-collapse SN model. Hence, we must be very cautious when drawing conclusions from a mixing-fraction analysis: the relevant parameter space and the uncertainties of current models are still utterly large.

5 CONCLUSIONS

We interfaced our semi-analytic codes `FASTCLUSTER` (Mapelli et al. 2021) and `COSMORATE` (Santoliquido et al. 2021). `FASTCLUSTER` dynamically pairs up binary black holes (BBHs) in dense star clusters, and integrates their orbital evolution via three-body hardening and gravitational-wave (GW) decay. With `FASTCLUSTER` we can study the dynamical formation of BBHs in very different star clusters, from the least massive young star clusters (YSCs) to the most massive globular clusters (GCs) and nuclear star clusters (NSCs). Furthermore, `FASTCLUSTER` includes a treatment for hierarchical mergers. `COSMORATE` calculates the BBH merger rate evolution, by using catalogues of BBH mergers simulated with `FASTCLUSTER` and by coupling them with the cosmic star formation rate and metallicity evolution. Here, we included the mass formation rate of NSCs, GCs and YSCs in `COSMORATE`.

We use `FASTCLUSTER + COSMORATE` to study four BBH formation channels: isolated BBHs and dynamical BBHs in NSCs, GCs and YSCs. This technique allows us to model different BBH formation channels with the same code, starting from the same BH mass function. Our approach prevents any systematic bias which arises from comparing outputs of different codes, that assume different stellar evolution models and BH mass function. We consider a large range of progenitor’s metallicities (twelve values of $Z \in [0.0002, 0.02]$), three values of the metallicity spread ($\sigma_Z = 0.2, 0.3$ and 0.4), two models of core-collapse SN (delayed and rapid), two values of the common envelope parameter ($\alpha = 1, 5$) and two models for the dimensionless spin χ (two truncated Maxwellian distributions with $\sigma_\chi = 0.01$ and 0.1).

We find a local BBH merger rate density $\mathcal{R}(0) \sim 4 - 8 \text{ Gpc}^{-3} \text{ yr}^{-1}$ in GCs. The BBH merger rate density in GCs increases up to redshift $z \sim 2.5 - 2.8$, reaching values ~ 6 times higher than the local merger rate density. The local merger rate density of BBHs in NSCs spans $\mathcal{R}(0) \sim 1 - 2 \text{ Gpc}^{-3} \text{ yr}^{-1}$. The rate associated with NSCs also peaks at $z \sim 2.5 - 2.8$, reaching values $\sim 4 - 5$ times higher than at $z = 0$ (Fig. 3).

The merger rate density of BBHs in both GCs and NSCs is very mildly affected by stellar metallicity, while the merger rate of isolated BBHs changes wildly with the metallicity spread σ_Z . BBHs in YSCs behave in an intermediate way between isolated BBHs and dynamical BBHs in GCs/NSCs. Enforcing or not the lower BH mass gap affects the merger rate density of all channels, from isolated BBHs to dynamical BBHs: the rapid core-collapse SN model (which prevents the formation of BHs with mass $< 5 M_\odot$) produces a higher merger rate by $\sim 40 - 60\%$ with respect to the delayed model (where we can have BHs with mass $3 - 5 M_\odot$). This happens because a higher minimum BH mass results in shorter delay times.

Our star cluster models grow a population of Nth generation (Ng) mergers. The local merger rate density of Ng BBHs is $\sim 0.8 - 2.5$, $\sim 0.5 - 1.0$, and $\sim 0.1 - 0.9 \text{ Gpc}^{-3} \text{ yr}^{-1}$ in GCs, NSCs and YSCs, respectively (Fig. 4). The total merger rate density of Ng BBHs in the local Universe, obtained by summing up these three channels, ranges from ~ 1 to $\sim 4 \text{ Gpc}^{-3} \text{ yr}^{-1}$ and is mostly sensitive to the spin parameter: we find higher (lower) values for our low-spin model with $\sigma_\chi = 0.01$ (fiducial model with $\sigma_\chi = 0.1$).

The primary BH mass function has a high-mass tail, extending up to several hundred M_\odot in the three dynamical channels, because of hierarchical mergers. The primary BH mass function evolves with redshift in both GCs and NSCs: lower mass BH mergers become less and less common at high redshift ($z \geq 1$), because they are associated with longer delay times (Fig. 5). In contrast, the primary BH mass function does not significantly evolve with redshift in iso-

lated BBHs, in agreement with previous studies (Mapelli et al. 2019; Santoliquido et al. 2020). This happens because binary evolution processes (e.g., common envelope) generate tight systems of low-mass BHs with short delay time (see, e.g., Mapelli et al. 2019). This difference has exciting implications for third-generation ground-based GW detectors: if Einstein Telescope and Cosmic Explorer will find a heavier BH mass function at higher redshift, this will be a signature that most BBH mergers have a dynamical origin; vice versa, isolated BBHs dominate the observed population if the mass function does not evolve with redshift.

The resulting primary BH mass function we obtain by combining our four channels according to their merger rate is similar to the `POWER LAW + PEAK` model used by the LIGO–Virgo–KAGRA collaboration (Abbott et al. 2021c). The main difference is that our models predict more BHs with mass $\sim 20 M_\odot$ with respect to the `POWER LAW + PEAK` model (Fig. 6). In our mass function, low-mass BHs are mostly given by isolated BBHs, YSCs and NSCs, while the high-mass tail ($\geq 50 M_\odot$) is mostly due to Ng BHs in GCs and NSCs.

The distribution of effective (χ_{eff}) and precessing (χ_p) spins we obtain by combining our four channels strongly depend on σ_χ . For $\sigma_\chi = 0.01$ (low-spin models), 1g BBHs have vanishingly small values of χ_{eff} . Hence, the effective spin distribution has a sharp peak at zero, surrounded by two symmetric broad wings due to Ng BBHs. The distribution of χ_p has two peaks: a primary peak, very narrow, at $\chi_p = 0$ and a secondary peak at $\chi_p \approx 0.7$, because of Ng BBHs. In contrast, for $\sigma_\chi = 0.1$, the distribution of effective spins becomes asymmetric: it peaks at $\chi_{\text{eff}} \approx 0.2$, because of isolated BBHs. In this case, the distribution of precessing spins has three peaks: a sharp primary peak at $\chi_p = 0$ because of isolated BBHs, a broader secondary peak at $\chi_p = 0.1 - 0.2$, because of 1g dynamical BBHs, and a third, lower peak at $\chi_p \sim 0.7$ because of Ng BBHs (Fig. 8).

We calculated the posterior probability distribution of the mixing fractions associated with our four channels, by running a Bayesian hierarchical analysis with posterior samples from GWTC-2 (Abbott et al. 2021b). The resulting mixing fractions indicate that at least two formation channels are likely at work to produce the observed BBH population (Fig. 9). However, the mixing fraction of each channel varies wildly from a model to another, being extremely sensitive to the metallicity spread σ_Z , the spin parameter σ_χ , the common envelope parameter α and the core-collapse SN model. Our models still suffer from large uncertainties (e.g. on the formation history of star clusters), but `FASTCLUSTER` and `COSMORATE` are extremely flexible and fast tool, and we can use them to probe the relevant parameter space.

ACKNOWLEDGEMENTS

MM, YB and FS acknowledge financial support from the European Research Council for the ERC Consolidator grant DEMOBLACK, under contract no. 770017. MCA and MM acknowledge financial support from the Austrian National Science Foundation through FWF stand-alone grant P31154-N27. MAS acknowledges financial support from the Alexander von Humboldt Foundation for the research program “The evolution of black holes from stellar to galactic scales”, the Volkswagen Foundation Trilateral Partnership through project No. I/97778, and the Deutsche Forschungsgemeinschaft (DFG) – Project-ID 138713538 – SFB 881.

DATA AVAILABILITY

The data underlying this article will be shared on reasonable request to the corresponding authors.

REFERENCES

- Aasi J., et al., 2015, *Classical and Quantum Gravity*, 32, 074001
- Abbott R., et al., 2020a, *Phys. Rev. Lett.*, 125, 101102
- Abbott R., et al., 2020b, *ApJ*, 900, L13
- Abbott R., et al., 2021a, arXiv e-prints, p. arXiv:2108.01045
- Abbott R., et al., 2021b, *Physical Review X*, 11, 021053
- Abbott R., et al., 2021c, *ApJ*, 913, L7
- Acernese F., et al., 2015, *Classical and Quantum Gravity*, 32, 024001
- Ade P. A. R., Aghanim N., Zonca A. e. a., 2016, *A&A*, 594, A13
- Ali-Haïmoud Y., Kovetz E. D., Kamionkowski M., 2017, *Phys. Rev. D*, 96, 123523
- Anagnostou O., Trenti M., Melatos A., 2020, arXiv e-prints, p. arXiv:2010.06161
- Antonini F., Gieles M., 2020a, *Phys. Rev. D*, 102, 123016
- Antonini F., Gieles M., 2020b, *MNRAS*, 492, 2936
- Antonini F., Rasio F. A., 2016, *ApJ*, 831, 187
- Antonini F., Capuzzo-Dolcetta R., Mastrobuono-Battisti A., Merritt D., 2012, *ApJ*, 750, 111
- Antonini F., Toonen S., Hamers A. S., 2017, *ApJ*, 841, 77
- Antonini F., Gieles M., Gualandris A., 2019, *MNRAS*, 486, 5008
- Arca Sedda M., 2020, *ApJ*, 891, 47
- Arca Sedda M., Mapelli M., Spera M., Benacquista M., Giacobbo N., 2020, *ApJ*, 894, 133
- Arca Sedda M., Rizzuto F. P., Naab T., Ostriker J., Giersz M., Spurzem R., 2021a, arXiv e-prints, p. arXiv:2105.07003
- Arca Sedda M., Li G., Kocsis B., 2021b, *A&A*, 650, A189
- Arca Sedda M., Amaro Seoane P., Chen X., 2021c, *A&A*, 652, A54
- Askar A., Szkudlarek M., Gondek-Rosińska D., Giersz M., Bulik T., 2017, *MNRAS*, 464, L36
- Baibhav V., Gerosa D., Berti E., Wong K. W. K., Helfer T., Mould M., 2020, *Phys. Rev. D*, 102, 043002
- Banerjee S., 2017, *MNRAS*, 467, 524
- Banerjee S., 2021, *MNRAS*, 500, 3002
- Banerjee S., Baumgardt H., Kroupa P., 2010, *MNRAS*, 402, 371
- Bartos I., Kocsis B., Haiman Z., Márka S., 2017, *ApJ*, 835, 165
- Bavera S. S., et al., 2020, *A&A*, 635, A97
- Belczynski K., 2020, *ApJ*, 905, L15
- Belczynski K., Kalogera V., Bulik T., 2002, *ApJ*, 572, 407
- Belczynski K., Kalogera V., Rasio F. A., Taam R. E., Zezas A., Bulik T., Maccarone T. J., Ivanova N., 2008, *ApJS*, 174, 223
- Belczynski K., Holz D. E., Bulik T., O’Shaughnessy R., 2016a, *Nature*, 534, 512
- Belczynski K., et al., 2016b, *A&A*, 594, A97
- Belczynski K., et al., 2020, *A&A*, 636, A104
- Belczynski K., et al., 2021, arXiv e-prints, p. arXiv:2108.10885
- Bethe H. A., Brown G. E., 1998, *ApJ*, 506, 780
- Binney J., Tremaine S., 1987, *Galactic dynamics*
- Bouffanais Y., Mapelli M., Gerosa D., Di Carlo U. N., Giacobbo N., Berti E., Baibhav V., 2019, *ApJ*, 886, 25
- Bouffanais Y., Mapelli M., Santoliquido F., Giacobbo N., Di Carlo U. N., Rastello S., Artale M. C., Iorio G., 2021, *MNRAS*,
- Breen P. G., Heggie D. C., 2013, *MNRAS*, 432, 2779
- Callister T. A., Farr W. M., Renzo M., 2020, arXiv e-prints, p. arXiv:2011.09570
- Campanelli M., Lousto C., Zlochower Y., Merritt D., 2007, *ApJ*, 659, L5
- Capuzzo-Dolcetta R., 1993, *ApJ*, 415, 616
- Capuzzo-Dolcetta R., Miocchi P., 2008, *MNRAS*, 388, L69
- Carr B. J., Hawking S. W., 1974, *MNRAS*, 168, 399
- Carr B., Kühnel F., Sandstad M., 2016, *Phys. Rev. D*, 94, 083504
- Chandrasekhar S., 1943, *ApJ*, 97, 255
- Chen Y., Bressan A., Girardi L., Marigo P., Kong X., Lanza A., 2015, *MNRAS*, 452, 1068
- Choksi N., Volonteri M., Colpi M., Gnedin O. Y., Li H., 2019, *ApJ*, 873, 100
- Chruslinska M., Nelemans G., Belczynski K., 2019, *MNRAS*, 482, 5012
- Clesse S., García-Bellido J., 2017, *Physics of the Dark Universe*, 15, 142
- Conselice C. J., Wilkinson A., Duncan K., Mortlock A., 2016, *ApJ*, 830, 83
- Costa G., Bressan A., Mapelli M., Marigo P., Iorio G., Spera M., 2021, *MNRAS*, 501, 4514
- De Luca V., Franciolini G., Pani P., Riotto A., 2021, *J. Cosmology Astropart. Phys.*, 2021, 003
- Di Carlo U. N., Giacobbo N., Mapelli M., Pasquato M., Spera M., Wang L., Haardt F., 2019, *MNRAS*, 487, 2947
- Di Carlo U. N., Mapelli M., Bouffanais Y., Giacobbo N., Santoliquido F., Bressan A., Spera M., Haardt F., 2020a, *MNRAS*, 497, 1043
- Di Carlo U. N., et al., 2020b, *MNRAS*, 498, 495
- Di Carlo U. N., et al., 2021, *MNRAS*,
- Doctor Z., Wysocki D., O’Shaughnessy R., Holz D. E., Farr B., 2020, *ApJ*, 893, 35
- Dvorkin I., Vangioni E., Silk J., Uzan J.-P., Olive K. A., 2016, *MNRAS*, 461, 3877
- Dvorkin I., Uzan J.-P., Vangioni E., Silk J., 2018, *MNRAS*, 479, 121
- El-Badry K., Quataert E., Weisz D. R., Choksi N., Boylan-Kolchin M., 2019, *MNRAS*, 482, 4528
- Eldridge J. J., Stanway E. R., 2016, *MNRAS*, 462, 3302
- Farmer R., Renzo M., de Mink S. E., Marchant P., Justham S., 2019, *ApJ*, 887, 53
- Farrell E., Groh J. H., Hirschi R., Murphy L., Kaiser E., Ekström S., Georgy C., Meynet G., 2021, *MNRAS*, 502, L40
- Favata M., Hughes S. A., Holz D. E., 2004, *ApJ*, 607, L5
- Fishbach M., Kalogera V., 2021, *ApJ*, 914, L30
- Fishbach M., Holz D. E., Farr B., 2017, *ApJ*, 840, L24
- Fishbach M., Holz D. E., Farr W. M., 2018, *ApJ*, 863, L41
- Fishbach M., et al., 2021, *ApJ*, 912, 98
- Fitchett M. J., 1983, *MNRAS*, 203, 1049
- Fragione G., Kocsis B., 2018, *Phys. Rev. Lett.*, 121, 161103
- Fragione G., Silk J., 2020, *MNRAS*, 498, 4591
- Fragione G., Loeb A., Rasio F. A., 2020, *ApJ*, 902, L26
- Fryer C. L., Belczynski K., Wiktorowicz G., Dominik M., Kalogera V., Holz D. E., 2012, *ApJ*, 749, 91
- Fujii M. S., Portegies Zwart S., 2014, *MNRAS*, 439, 1003
- Gallegos-Garcia M., Berry C. P. L., Marchant P., Kalogera V., 2021, arXiv e-prints, p. arXiv:2107.05702
- Georgiev I. Y., Puzia T. H., Hilker M., Goudfrooij P., 2009a, *MNRAS*, 392, 879
- Georgiev I. Y., Hilker M., Puzia T. H., Goudfrooij P., Baumgardt H., 2009b, *MNRAS*, 396, 1075
- Georgiev I. Y., Böker T., Leigh N., Lützgendorf N., Neumayer N., 2016, *MNRAS*, 457, 2122
- Gerosa D., Berti E., 2017, *Phys. Rev. D*, 95, 124046
- Gerosa D., Fishbach M., 2021, *Nature Astronomy*,
- Gerosa D., Giacobbo N., Vecchio A., 2021, *ApJ*, 915, 56
- Giacobbo N., Mapelli M., 2018, *MNRAS*, 480, 2011
- Giacobbo N., Mapelli M., 2020, *ApJ*, 891, 141
- Giacobbo N., Mapelli M., Spera M., 2018, *MNRAS*, 474, 2959
- Giersz M., Leigh N., Hypki A., Lützgendorf N., Askar A., 2015, *MNRAS*, 454, 3150
- González E., Kremer K., Chatterjee S., Fragione G., Rodriguez C. L., Weatherford N. C., Ye C. S., Rasio F. A., 2021, *ApJ*, 908, L29
- Goodman J., Hut P., 1993, *ApJ*, 403, 271
- Gräfener G., Hamann W.-R., 2008, *A&A*, 482, 945
- Gratton R. G., Fusi Pecci F., Carretta E., Clementini G., Corsi C. E., Lattanzi M., 1997, *ApJ*, 491, 749
- Gratton R. G., Bragaglia A., Carretta E., Clementini G., Desidera S., Grundahl F., Lucatello S., 2003, *A&A*, 408, 529
- Harris W. E., 1996, *AJ*, 112, 1487
- Heger A., Fryer C. L., Woosley S. E., Langer N., Hartmann D. H., 2003, *ApJ*, 591, 288
- Heggie D. C., 1975, *MNRAS*, 173, 729

- Hills J. G., 1983, *AJ*, **88**, 1269
- Holley-Bockelmann K., Gülltekin K., Shoemaker D., Yunes N., 2008, *ApJ*, **686**, 829
- Hong J., Vesperini E., Askar A., Giersz M., Szkudlarek M., Bulik T., 2018, *MNRAS*, **480**, 5645
- Hurley J. R., Tout C. A., Pols O. R., 2002, *MNRAS*, **329**, 897
- Ishibashi W., Gröbner M., 2020, *A&A*, **639**, A108
- Ji J., Bregman J. N., 2015, *ApJ*, **807**, 32
- Jiménez-Forteza X., Keitel D., Husa S., Hannam M., Khan S., Pürrer M., 2017, *Phys. Rev. D*, **95**, 064024
- Kamlah A. W. H., et al., 2021, arXiv e-prints, p. arXiv:2105.08067
- Kimball C., Talbot C., Berry C. P. L., Carney M., Zevin M., Thrane E., Kalogera V., 2020, *ApJ*, **900**, 177
- Kimball C., et al., 2021, *ApJ*, **915**, L35
- Klencki J., Moe M., Gladysz W., Chruslinska M., Holz D. E., Belczynski K., 2018, *A&A*, **619**, A77
- Klencki J., Nelemans G., Istrate A. G., Chruslinska M., 2021, *A&A*, **645**, A54
- Kremer K., et al., 2020a, *ApJS*, **247**, 48
- Kremer K., et al., 2020b, *ApJ*, **903**, 45
- Kroupa P., 2001, *MNRAS*, **322**, 231
- Kruckow M. U., Tauris T. M., Langer N., Kramer M., Izzard R. G., 2018, *MNRAS*, **481**, 1908
- Krujssens J. M. D., 2014, *Classical and Quantum Gravity*, **31**, 244006
- Kumamoto J., Fujii M. S., Tanikawa A., 2019, *MNRAS*, **486**, 3942
- Kumamoto J., Fujii M. S., Tanikawa A., 2020, *MNRAS*, **495**, 4268
- Lada C. J., Lada E. A., 2003, *ARA&A*, **41**, 57
- Lee H. M., 1995, *MNRAS*, **272**, 605
- Liu B., Lai D., 2021, *MNRAS*, **502**, 2049
- Loredó T. J., 2004, *AIP Conf. Proc.*, **735**, 195
- Lousto C. O., Zlochower Y., 2011, *Phys. Rev. Lett.*, **107**, 231102
- Lousto C. O., Zlochower Y., Dotti M., Volonteri M., 2012, *Phys. Rev. D*, **85**, 084015
- Madau P., Fragos T., 2017, *ApJ*, **840**, 39
- Mandel I., Broekgaarden F. S., 2021, arXiv e-prints, p. arXiv:2107.14239
- Mandel I., de Mink S. E., 2016, *MNRAS*, **458**, 2634
- Mandel I., Farr W. M., Gair J. R., 2019, *MNRAS*, **486**, 1086
- Mapelli M., 2016, *MNRAS*, **459**, 3432
- Mapelli M., 2021, arXiv e-prints, p. arXiv:2106.00699
- Mapelli M., Hayfield T., Mayer L., Wadsley J., 2012, *ApJ*, **749**, 168
- Mapelli M., Giacobbo N., Ripamonti E., Spera M., 2017, *MNRAS*, **472**, 2422
- Mapelli M., Giacobbo N., Santoliquido F., Artale M. C., 2019, *MNRAS*, **485**, 889
- Mapelli M., Spera M., Montanari E., Limongi M., Chieffi A., Giacobbo N., Bressan A., Bouffanais Y., 2020, *ApJ*, **888**, 76
- Mapelli M., et al., 2021, *MNRAS*, **505**, 339
- Marchant P., Langer N., Podsiadlowski P., Tauris T. M., Moriya T. J., 2016, *A&A*, **588**, A50
- Marchant P., Renzo M., Farmer R., Pappas K. M. W., Taam R. E., de Mink S. E., Kalogera V., 2019, *ApJ*, **882**, 36
- McKernan B., et al., 2018, *ApJ*, **866**, 66
- Miller M. C., Hamilton D. P., 2002, *MNRAS*, **330**, 232
- Miller M. C., Lauburg V. M., 2009, *ApJ*, **692**, 917
- Milone A. P., et al., 2012, *A&A*, **540**, A16
- Moody K., Sigurdsson S., 2009, *ApJ*, **690**, 1370
- Neijssel C. J., et al., 2019, *MNRAS*, **490**, 3740
- Neumayer N., Seth A., Böker T., 2020, *A&ARv*, **28**, 4
- Ng K. K. Y., Vitale S., Farr W. M., Rodriguez C. L., 2021, *ApJ*, **913**, L5
- O’Leary R. M., Meiron Y., Kocsis B., 2016, *ApJ*, **824**, L12
- Olejak A., Belczynski K., Ivanova N., 2021, *A&A*, **651**, A100
- Peters P. C., 1964, *Physical Review*, **136**, 1224
- Petrovich C., Antonini F., 2017, *ApJ*, **846**, 146
- Portegies Zwart S. F., McMillan S. L. W., 2000, *ApJ*, **528**, L17
- Portegies Zwart S. F., Yungelson L. R., 1998, *A&A*, **332**, 173
- Portegies Zwart S. F., McMillan S. L. W., Gieles M., 2010, *ARA&A*, **48**, 431
- Quinlan G. D., 1996, *New Astron.*, **1**, 35
- Rastello S., Mapelli M., Di Carlo U. N., Iorio G., Ballone A., Giacobbo N., Santoliquido F., Tornamenti S., 2021, *MNRAS*, **507**, 3612
- Reina-Campos M., Kruijssens J. M. D., Pfeffer J. L., Bastian N., Crain R. A., 2019, *MNRAS*, **486**, 5838
- Renzo M., Cantiello M., Metzger B. D., Jiang Y. F., 2020, *ApJ*, **904**, L13
- Riley J., Mandel I., Marchant P., Butler E., Nathaniel K., Neijssel C., Shortt S., Vigna-Gómez A., 2021, *MNRAS*, **505**, 663
- Rizzuto F. P., et al., 2021, *MNRAS*, **501**, 5257
- Rodriguez C. L., Loeb A., 2018, *ApJ*, **866**, L5
- Rodriguez C. L., Chatterjee S., Rasio F. A., 2016, *Phys. Rev. D*, **93**, 084029
- Rodriguez C. L., Zevin M., Amaro-Seoane P., Chatterjee S., Kremer K., Rasio F. A., Ye C. S., 2019, *Phys. Rev. D*, **100**, 043027
- Roulet J., Chia H. S., Olsen S., Dai L., Venumadhav T., Zackay B., Zaldarriaga M., 2021, arXiv e-prints, p. arXiv:2105.10580
- Samsing J., 2018, *Phys. Rev. D*, **97**, 103014
- Samsing J., MacLeod M., Ramirez-Ruiz E., 2014, *ApJ*, **784**, 71
- Sana H., et al., 2012, *Science*, **337**, 444
- Santoliquido F., Mapelli M., Bouffanais Y., Giacobbo N., Di Carlo U. N., Rastello S., Artale M. C., Ballone A., 2020, *ApJ*, **898**, 152
- Santoliquido F., Mapelli M., Giacobbo N., Bouffanais Y., Artale M. C., 2021, *MNRAS*, **502**, 4877
- Sasaki M., Suyama T., Tanaka T., Yokoyama S., 2016, *Physical Review Letters*, **117**, 061101
- Sesana A., Haardt F., Madau P., 2006, *ApJ*, **651**, 392
- Silber K., Tremaine S., 2017, *ApJ*, **836**, 39
- Sollima A., Beccari G., Ferraro F. R., Fusi Pecci F., Sarajedini A., 2007, *MNRAS*, **380**, 781
- Spera M., Mapelli M., 2017, *MNRAS*, **470**, 4739
- Spera M., Mapelli M., Giacobbo N., Trani A. A., Bressan A., Costa G., 2019, *MNRAS*, **485**, 889
- Spitzer Jr. L., 1969, *ApJ*, **158**, L139
- Stevenson S., Berry C. P. L., Mandel I., 2017, *MNRAS*, **471**, 2801
- Stevenson S., Sampson M., Powell J., Vigna-Gómez A., Neijssel C. J., Szécsi D., Mandel I., 2019, *ApJ*, **882**, 121
- Stone N. C., Metzger B. D., Haiman Z., 2017, *MNRAS*, **464**, 946
- Tagawa H., Haiman Z., Kocsis B., 2020, *ApJ*, **898**, 25
- Tanikawa A., 2013, *MNRAS*, **435**, 1358
- Tanikawa A., Kinugawa T., Yoshida T., Hijikawa K., Umeda H., 2021, *MNRAS*, **505**, 2170
- Tremaine S. D., Ostriker J. P., Spitzer L. J., 1975, *ApJ*, **196**, 407
- Tutukov A., Yungelson L., 1973, *Nauchnye Informatsii*, **27**, 70
- VandenBerg D. A., Brogaard K., Leaman R., Casagrande L., 2013, *ApJ*, **775**, 134
- Vigna-Gómez A., Toonen S., Ramirez-Ruiz E., Leigh N. W. C., Riley J., Haster C.-J., 2021, *ApJ*, **907**, L19
- Vink J. S., de Koter A., Lamers H. J. G. L. M., 2001, *A&A*, **369**, 574
- Vink J. S., Higgins E. R., Sander A. A. C., Sabhahit G. N., 2021, *MNRAS*, **504**, 146
- Wang L., 2020, *MNRAS*, **491**, 2413
- Ward J. L., Kruijssens J. M. D., Rix H.-W., 2020, *MNRAS*, **495**, 663
- Wong K. W. K., Breivik K., Kremer K., Callister T., 2021, *Phys. Rev. D*, **103**, 083021
- Woosley S. E., 2017, *ApJ*, **836**, 244
- Yang Y., Bartos I., Haiman Z., Kocsis B., Márka Z., Stone N. C., Márka S., 2019, *ApJ*, **876**, 122
- Zevin M., Pankow C., Rodriguez C. L., Sampson L., Chase E., Kalogera V., Rasio F. A., 2017, *ApJ*, **846**, 82
- Zevin M., Samsing J., Rodriguez C., Haster C.-J., Ramirez-Ruiz E., 2019, *ApJ*, **871**, 91
- Zevin M., et al., 2021, *ApJ*, **910**, 152
- Ziosi B. M., Mapelli M., Branchesi M., Tormen G., 2014, *MNRAS*, **441**, 3703
- de Mink S. E., Mandel I., 2016, *MNRAS*, **460**, 3545
- du Buisson L., et al., 2020, *MNRAS*, **499**, 5941